CHARACTERIZATION OF MICROSTRUCTURED SURFACE TEXTURE USING ANGLE-RESOLVED SCATTERING

A THESIS SUBMITTED TO
THE GRADUATE SCHOOL OF NATURAL AND APPLIED SCIENCES
OF
MIDDLE EAST TECHNICAL UNIVERSITY

BY

NURAY BAŞARAN

IN PARTIAL FULFILLMENT OF THE REQUIREMENTS
FOR
THE DEGREE OF MASTER OF SCIENCE
IN
MICRO AND NANOTECHNOLOGY

APRIL 2025

Approval of the thesis:

CHARACTERIZATION OF MICROSTRUCTURED SURFACE TEXTURE USING ANGLE-RESOLVED SCATTERING

submitted by **NURAY BAŞARAN** in partial fulfillment of the requirements for the degree of **Master of Science** i**n Micro and Nanotechnology, Middle East Technical University** by,

Prof. Dr. Naci Emre Altun
Dean, **Graduate School of Natural and Applied Sciences** _____

Prof. Dr. Hüsnü Emrah Ünalan
Head of the Department, **Micro and Nanotechnology** _____

Prof. Dr. Alpan Bek
Supervisor, **Micro and Nanotechnology, METU** _____

Dr. Amir Ghobadi
Co-Supervisor, **NANOTAM, I. D. Bilkent University** _____

Examining Committee Members:

Prof. Dr. Burcu Akata Kurç
Micro and Nanotechnology, METU _____

Prof. Dr. Alpan Bek
Physics, METU _____

Prof. Dr. Halil Berberoğlu
Physics, Ankara Haci Bayram Veli University _____

Prof. Dr. Okan Esentürk
Chemistry, METU _____

Assist. Prof. Dr. Yusuf Keleştemur
Metallurgical and Materials Engineering, METU _____

Date: 17.04.2025

I hereby declare that all information in this document has been obtained and presented in accordance with academic rules and ethical conduct. I also declare that, as required by these rules and conduct, I have fully cited and referenced all material and results that are not original to this work.

Name Last name :

Signature :

ABSTRACT

CHARACTERIZATION OF MICROSTRUCTURED SURFACE TEXTURE USING ANGLE-RESOLVED SCATTERING

Başaran, Nuray
Master of Science, Micro and Nanotechnology
Supervisor: Prof. Dr. Alpan Bek
Co-Supervisor: Dr. Amir Ghobadi

April 2025, 88 pages

Accurate characterization of microstructured surfaces is essential for evaluating their optical performance, particularly in applications involving light scattering, sensing, and anti-reflective engineering. This study presents a systematic investigation of angularly resolved scattering (ARS) from laser-textured silicon surfaces to extract structural information at the microscale. A custom-built ARS measurement setup was employed to record the intensity distribution of reflected light as a function of scattering angle, with the illumination fixed at 45° incidence. The samples comprised both periodic (grating-like) and aperiodic (rough) surface morphologies, fabricated by varying femtosecond laser processing parameters.

To validate and interpret the scattering profiles, two complementary approaches were utilized: frequency-domain analysis of surface topography via 2D Fast Fourier

Transform (FFT) on SEM and AFM images, and angular-domain analysis of optical scattering patterns. Periodic samples exhibited distinct diffraction orders, and the extracted peak positions were used to estimate spatial periods via the grating equation, which closely matched FFT results. In contrast, rougher surfaces fabricated at higher laser powers displayed broadened angular profiles, increased diffuse background levels, and the absence of well-defined diffraction orders. Extended scans over 10°–120°, centered around the specular reflection angle, revealed how increasing surface irregularity leads to loss of angular coherence and redistribution of scattered intensity.

The combined optical and morphological analyses confirm that ARS provides a sensitive, non-destructive tool for quantifying both periodicity and surface roughness. The findings also highlight the strong correlation between laser processing conditions and the evolution of surface texture, bridging the gap between fabrication parameters and optical functionality.

Keywords: Angle-Resolved Scattering, Diffraction Theory, Surface Periodicity Analysis, Microstructured Surfaces, Optical Characterization

ÖZ

AÇIYA BAĞLI SAÇILMA YÖNTEMİYLE MİKROYAPILI YÜZEY DOKULARININ KARAKTERİZASYONU

Başaran, Nuray
Yüksek Lisans, Mikro ve Nanoteknoloji
Tez Yöneticisi: Prof. Dr. Alpan Bek
Ortak Tez Yöneticisi: Dr. Amir Ghobadi

Nisan 2025, 88 sayfa

Mikroyapılı yüzeylerin doğru bir şekilde karakterize edilmesi, özellikle ışık saçılması, algılama ve yansıtma önleyici mühendislik gibi uygulamalarda optik performansın değerlendirilmesi açısından kritik öneme sahiptir. Bu çalışmada, mikroskobik ölçekte yapısal bilgi elde etmek amacıyla, lazerle işlenmiş silisyum yüzeylerden alınan açısal çözünürlüklü saçılma (ARS) verileri sistematik olarak incelenmiştir. 45° sabit gelme açısıyla aydınlatılan özel tasarlanmış bir ARS sistemi kullanılarak, yansıyan ışığın saçılma açısına bağlı olarak şiddet dağılımı ölçülmüştür. Numuneler, femtosaniye lazerle farklı işleme parametreleri uygulanarak üretilmiş periyodik (ızgara benzeri) ve düzensiz (pürüzlü) yüzey morfolojilerinden oluşmaktadır.

Saçılma profillerini doğrulamak ve yorumlamak amacıyla iki tamamlayıcı yaklaşım kullanılmıştır: SEM ve AFM görüntüleri üzerinde uygulanan 2B Hızlı Fourier

Dönüşümü (FFT) ile yapılan frekans domeni analizi ve optik saçılma desenlerinin açısal analizleri. Periyodik numunelerde belirgin kırınım basamakları gözlenmiş ve bu tepe noktalarının konumları, ızgara denklemi kullanılarak yüzey periyotlarının tahmin edilmesinde kullanılmış; elde edilen sonuçlar FFT ile elde edilen değerlerle yüksek uyum göstermiştir. Buna karşılık, daha yüksek lazer güçleriyle üretilen pürüzlü yüzeyler, daha geniş açılı saçılma profilleri, artmış yayılma seviyesi ve belirgin kırınım basamaklarının yokluğu ile karakterize edilmiştir. Speküler yansıma açısı etrafında (10°–120°) yapılan geniş açılı taramalar, artan yüzey düzensizliğinin açısal koherensi nasıl bozduğunu ve saçılan ışığın nasıl yeniden dağıldığını ortaya koymuştur.

Elde edilen optik ve morfolojik analizler, ARS yönteminin hem periyodiklik hem de yüzey pürüzlülüğünü nicel olarak belirleyebilen duyarlı ve tahribatsız bir yöntem olduğunu doğrulamaktadır. Ayrıca bulgular, lazerle işleme koşulları ile yüzey dokusunun evrimi arasındaki güçlü ilişkiyi vurgulayarak, üretim parametreleri ile optik işlevsellik arasındaki bağı güçlendirmektedir.

Anahtar Kelimeler: Açısal Çözünürlüklü Saçılma, Kırınım Teorisi, Yüzey Periyotluğu Analizi, Mikro Yapılandırılmış Yüzeyler, Optik Karakterizasyon

In loving memory of Tontiki, whom I recently lost

My honey-foam girl

ACKNOWLEDGMENTS

First and foremost, I would like to express my deepest gratitude to my supervisor, Prof. Dr. Alpan Bek. His mentorship has been the greatest fortune of my academic life at METU. For the past ten years, he has always believed in me, supported me through every step, especially the uncertain and faltering ones, and consistently encouraged me to pursue my own path. I have always admired his patience, curiosity, and the sense of confidence he so generously imparts.

I would also like to extend my heartfelt thanks to Prof. Dr. Altuğ Özpineci. The perspective he helped me gain towards life is something I could never have acquired elsewhere. His wisdom and presence have had a lasting impact beyond academics.

I sincerely thank my thesis jury members, Prof. Dr. Burcu Akata Kurç, Prof. Dr. Halil Berberoğlu, Prof. Dr. Okan Esentürk, and Assist. Prof. Dr. Yusuf Keleştemur, for their thoughtful questions, constructive feedback, and kind encouragement throughout the process. Their insights made everything more meaningful.

Special thanks to Zeynep Cantürk and İlayda Alparslan for their dedicated efforts in sample fabrication; to Batuhan Bürhan for his invaluable support; Cem Maden and Salar Sedani for their help with AFM measurements; and to Batuhan Balkan and Rana Akyazı for always being willing to help with anything in the lab. I am also grateful to Mete Günöven for his help when I was stuck. Warm thanks to Ulvi Nohutçu for his encouragement and conversation always brightened my day.

I am deeply grateful to Melahat Yapıcı, who has been by my side since high school and whom I trust in every aspect of life, for her helps, support and motivation throughout this journey; to Cemre Uyar, for the questions that made us laugh, and the smile that warmed our hearts; Asya Polat, who was always there for me without hesitation; Faruk Kurtuluş, for his incredibly kind and compassionate heart; and Alper Karasuer, always curious and fun to debate with.

Heartfelt thanks to Gizem Ayaz and Şevval Koç, whose support during a difficult time helped me stay focused on my thesis.

I deeply admire and thank Sümeyye Şimşek for her courage and unwavering justice sense; Başak Kabaloğlu, her determination and laughter will always stay with me; Şilan Akyol, bright in mind and stubborn at heart, I cared deeply, never figured out, always understood; and my captains; Hatice Şahin for her inspiring work ethic and discipline, and Ceylin Ökten for revealing life's beauty with her adventurous spirit. Meryem Çiftçi, Ezgi Yıldız, Asiye Anralıgil, Esma Kabukçu, Buse Güllüoğlu, Nisanur Tekin, Ece Canbaz, Maide Şirin and Ayşe Tüysüz, whose quick feet once dribbled past me easily (now not quite as easily) and kind hearts made everything special. Last but certainly not least, forever grateful to coach Özgür Norman, who has patiently guided me since 2018, always believed in our potential, never gave up on us. To all my METU Women's Futsal teammates and coach: so much to admire, too little space. It was never about winning or losing but effort and laughter meant the world to me and always echoes within. May your kindness, love, and team spirit last forever, because I will carry them always.

I owe my deepest thanks to my parents and sisters, for shaping who I am, teaching me how to fight through hardship, and always standing by my side. Even in the hardest times, we held on to each other. That's the greatest lesson I've learned from you: to keep fighting, and to be there for the people you love, no matter the struggle between you.

And finally… To my beloved cat, Tontiki, whom I lost recently. For five years, you were the gentlest soul in my life, my friend, my daughter, my little source of light. I never imagined losing you. Your curious spirit, your joy in every meal, your bright, life-filled eyes… You were so full of life… You taught me how to find delight in this world. My love and longing for you are more than words can tell. Now it's just us and your brother Miskin, missing you every day. I will carry you with me, always, my honey-foam girl.

TABLE OF CONTENTS

LIST OF TABLES

TABLES

LIST OF FIGURES

FIGURES

LIST OF ABBREVIATIONS

ABBREVIATIONS

ADC	**:**	Analog-to-Digital Converter
AFM	**:**	Atomic Force Microscope
ARS	**:**	Angle-Resolved Scattering
DC	**:**	Direct Current (or zero-frequency component in FFT context)
EM	**:**	Electromagnetic
FFT	**:**	Fast Fourier Transform
FWHM	**:**	Full Width at Half Maximum
LIPSS	**:**	Laser-Induced Periodic Surface Structuring
nm	**:**	Nanometer
SEM	**:**	Scanning Electron Microscope
µm	**:**	Micrometer

LIST OF SYMBOLS

SYMBOLS

A	:	Absorption
d	:	Grating period (surface periodicity)
E	:	Electric field amplitude
$\vec{\mathbf{E}}$	:	Vector electric field
H	:	Magnetic field amplitude
$\vec{\mathbf{H}}$	:	Vector magnetic field
I(θ)	:	Scattered light intensity as a function of angle
k	:	Wave number $k = 2\pi / \lambda$
m	:	Diffraction order
n	:	Refractive index of a medium
ñ	:	Complex refractive index $\tilde{n} = n + i\kappa$
θ	:	General angle (e.g., scattering or measurement angle)
θ_i	:	Angle of incidence
θ_m	:	Angle of m-th diffraction order relative to surface normal
ω	:	Angular frequency of the incident wave
R	:	Reflection coefficient
σ	:	Standard deviation (in statistical/optical analysis)
T	:	Transmission coefficient
x	:	Dimensionless size parameter $x = 2\pi d / \lambda$
ε	:	Electric permittivity
κ	:	Extinction coefficient
λ	:	Wavelength of the incident light
μ	:	Magnetic permeability

CHAPTER 1

INTRODUCTION

The investigation of the optical characteristics and functionality of micro- and nanoscale surfaces has grown in significance for scientific and technological advancements in recent decades. The interaction mechanisms between electromagnetic waves and matter are consequently critical for understanding the optical behaviour of micro- and nanoscale surface characteristics[1]. When electromagnetic radiation interacts with a material, it can be reflected, scattered, refracted or absorbed [2]. Depending on the type of material, surface morphology, roughness level, chemical composition, permeability and reflectivity, the interaction with the surface can result in different outcomes [3]. Detailed and accurate consideration of the behavior of materials under light exposure is essential for various modern technology applications. It is critical for the effective and appropriate design of optical devices and systems [4]. Determining and optimizing the reflectivity of surfaces enhances the energy efficiency of optical systems, while optimizing the sensitivity of optical sensors further improves their performance[5]. In addition, understanding how structured surfaces interact with light can greatly contribute to improving the efficiency of solar cells and the design of photonic devices [6]. Understanding and controlling optical behaviour and surface morphology, such as roughness and nanostructuring, in solar cells is critical for maximising light absorption and minimising reflection losses, which directly improves power conversion efficiency [7]. Surface characteristics in photonic devices have a significant impact on light propagation, confinement, and interference, requiring careful control of optical responses to achieve desired functionality and spectral performance [8].

Research on optical scattering began in the late 19th and early 20th centuries, particularly through the works of Lord Rayleigh and Gustav Mie [9]. Their theories detailed how electromagnetic waves interact with particles and surfaces, laying the foundation for modern optics research. Over time, improvements in optics have been aimed at characterizing the surfaces of more complex structures. For this reason, the Angle Resolved Scattering (ARS) method has been developed [10] since the mid-20th century. ARS is a widely used method in optics research that analyzes surfaces by measuring scattered radiation intensity at different angles. In modern optics research, the ARS technique has become essential for precise measurements of micro- and nanoscale structures [11].

Optical scattering as a function of angle is an effective, inexpensive and rapid method for characterizing micro and nanoscale periodic surface structures. The intensity distribution of scattered light relates to the size, shape, and arrangement of periodic structures on the surface[12], establishing an accurate and direct relationship between scattering patterns and structural parameters.

1.1 Laser Scattering

Laser scattering is an effective method used to analyze surface properties by examining how a laser beam interacts with a structured surface [13]. While conventional electromagnetic wave sources emit a broad wavelength spectrum and are incoherent and divergent; lasers are monochromatic, coherent and collimated [14]. Therefore, using laser for scattering measurements can be more efficient because it provides precision and control. These properties ensure that laser scattering enables high-resolution, non-contact surface characterization [15], making it particularly suitable for micro- and nanoscale applications.

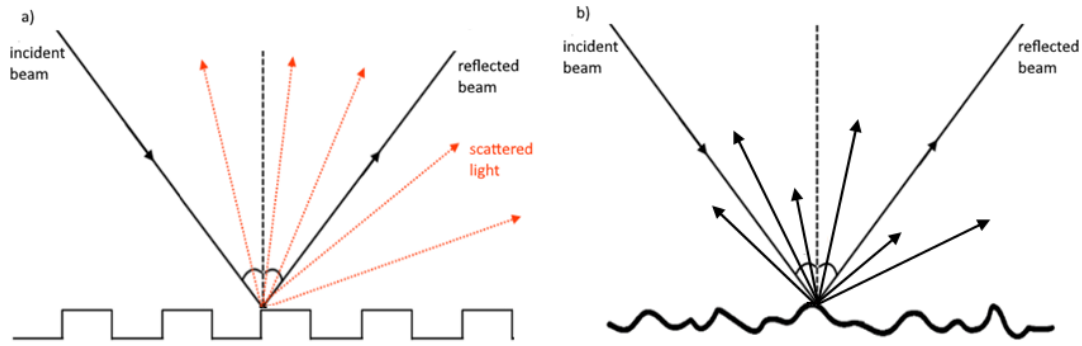

Figure 1.1 a) Scattering from periodic surface and b) rough surface

On a flat surface, the incoming light is reflected in a single direction as a sharp beam, whereas on a textured surface, it is scattered into multiple directions due to surface features, as illustrated in Figure 1.1a) and Figure 1.1b) respectively. This angular spread is the main idea behind angle-resolved scattering measurements [16].

1.2 Angle Resolved Scattering (ARS)

ARS is an optical characterization technique that provides information by utilizing the angular distribution of light for the analysis of surface properties [17]. Light interacting with the surface is scattered at different angles and different intensities depending on the surface properties. Examining the periodicity, roughness and defects on the surface according to the intensity and angular distribution of the scattered light can be achieved with high accuracy [18], [19].

It should be underlined that, compared to other characterization techniques such as Atomic Force Microscopy (AFM) and Scanning Electron Microscopy (SEM), ARS has significant advantages [20]. ARS allows for fast and reliable surface measurements without direct contact with the sample, minimizing damage and enabling rapid characterization of large areas [18]. Laser scattering is highly effective in detecting sub-wavelength variations in surface roughness and periodicity. It provides the opportunity to learn surface properties quickly at the time of scanning and it ensures precise localization of the measurement region. In this

way, it is an efficient and practical measurement tool method that provides a lot of information in a short time for optical and semiconductor production and precision engineering applications.

1.3 Scope of the Study

The primary goal of this study is to develop and validate a practical and non-destructive optical method for characterizing surface textures at the microscale using ARS. This method aims to reveal critical surface features such as periodicity, structural coherence, and roughness-induced irregularities through optical signatures, without requiring direct contact, extensive sample preparation, or expensive instrumentation.

By designing a custom-built ARS system and applying it to a variety of laser-textured silicon surfaces, this study investigates whether scattering profiles can reflect morphological differences in a consistent and interpretable way.

evaluating surface uniformity based on the consistency of specular reflection and surrounding angular features,

The analysis focuses on three main aspects:

1. Evaluating surface uniformity based on the consistency of specular reflection and the surrounding angular features,
2. Identifying periodic structures through diffraction peaks and comparing them to spatial frequencies obtained from FFT analysis of SEM images,
3. Assessing surface roughness by analyzing background levels, peak broadening, and wide-angle scattering behavior, and relating them to morphological indicators observed in AFM and SEM data.

Although there are numerous studies on the optical analysis of surface roughness and scattering-based defect inspection [12], [21] research focusing on characterizing periodic structures on micro-perforated or laser-structured surfaces using ARS is

relatively limited in the current literature [22]. This study addresses that gap by demonstrating how angular scattering measurements can be used to extract structural information from engineered surfaces with high accuracy and reliability.

The overall aim is to demonstrate that angular scattering measurements, when properly interpreted, can offer a fast, cost-effective, and reproducible way to characterize surface quality. The developed method not only complements traditional imaging techniques like SEM and AFM [23] but also provides a scalable route for high-throughput surface screening.

The main purpose of this study is to identify periodic structures on micro-perforated surfaces by analyzing their angle-dependent scattering properties and to determine their dimensions and characteristics with high accuracy and reliability. Both theoretical and computational approaches will be used to interpret and analyze the experimental data obtained from measurements performed with the ARS technique.

CHAPTER 2

THEORETICAL BACKGROUND

2.1 Electromagnetic Wave Interaction with Structured Surfaces

When electromagnetic waves interact with a solid surface, optical behavior depends both on the intrinsic properties of materials and on the structural characteristics of the surface [24]. These interactions include reflection, absorption, and scattering, all of which are influenced by the surface morphology, roughness, and texture [25]. These effects form the basis of more complex optical phenomena such as diffraction and angular scattering, which are closely related to the structural features of the surface.

2.1.1 Fundamental Optical Mechanisms at the Interface

During the interaction of an electromagnetic wave with a surface, the electric and magnetic fields at the interface must satisfy the boundary conditions. These boundary conditions can be derived from Maxwell's equations [26] (2.1), (2.2) and they allow us to understand how much of the incident light is reflected, how much is transmitted by the material, and how much energy is lost through absorption. In particular, the boundary conditions used to determine reflected and transmitted fields at material interfaces are derived from Faraday’s law (2.1) and Ampère–Maxwell law (2.2) [27]. The refractive index contrast and the angle of incidence determine the reflection and transmission coefficients, which control the quantitative description of the amount of light that is reflected or transmitted [28].

$$\nabla \times \vec{E} = -\frac{\partial \vec{B}}{\partial t} \tag{2.1}$$

$$\nabla \times \vec{B} = \mu_0 \vec{J} + \mu_0 \epsilon_0 \frac{\partial \vec{E}}{\partial t} \tag{2.2}$$

At the microscopic level, the incident wave induces oscillations in the bound electrons of atoms or molecules within the material [29]. These oscillating dipoles emit secondary wavelets in all directions. At sharp interfaces, the backward-propagating wavelets from near-surface dipoles are no longer canceled by symmetrical neighbors, and their constructive interference gives rise to the reflected wave. In structured or rough surfaces, the interaction becomes more complex compared to flat and homogeneous interfaces. The scattered light spreads over a broader angular range, creating more diverse intensity profiles.

According to the law of reflection, the angle of incident light and the angle of reflection relative to the surface normal are equal [30]. This relationship is important for using specular reflection as a reference in our angle-resolved scattering measurements.

Absorption occurs when the energy of the incident photons matches an electronic transition in the atoms or molecules of the material [31]. In such cases, the incident wave is not re-emitted but is transformed into different forms of energy, such as thermal energy. Even if the energy of the photon is not exactly resonant, the oscillating electric field can still induce dipole oscillations in [32] bound electrons. In dense materials, these oscillations often result in energy loss through non-radiative damping mechanisms. This absorption power increases as the wavelength approaches the resonant frequency of the material [33].

On micro-perforated silicon surfaces or laser-textured structured samples, angular scattering behavior can vary significantly due to the combined effects of surface geometry, absorption, and refraction properties [34]. These variations directly influence angular distribution and intensity profiles of scattered and reflected light. A decrease in intensity of specular reflection and redistribution of light to wider

angles can indicate enhanced light-trapping behavior, which is especially desirable in solar cell applications [35].

The Fresnel equations [36] describe how much of the incident electromagnetic wave is reflected and how much is transmitted at the boundary between two media with different refractive indices. These equations are derived by applying the boundary conditions of Maxwell's equations (2.1), (2.2), which require the continuity of the tangential components of the electric and magnetic fields across the interface. Fresnel equations vary depending on the polarization of the incident wave. However, in this study, polarization was not varied or analyzed separately. Therefore, a general form (Eq.2.3) of the reflection coefficient is considered to understand the interaction of light with surfaces.

$$R = \left|\frac{n_1 cos\theta_i - n_2 cos\theta_t}{n_1 cos\theta_i + n_2 cos\theta_t}\right|^2 \tag{2.3}$$

θ_i is the angle of incidence, θ_t is the angle of transmission.

2.1.2 Material Properties and Optical Response

The optical behavior of a material is mainly determined by its refractive index (n) and extinction coefficient (k) [37]. A higher n value leads to stronger refraction of light, while a higher k value indicates more absorption within medium. The optical response is described by the complex refractive index, as shown in Eq. (2.4)

$$\tilde{n} = n + ik \tag{2.4}$$

In addition to intrinsic material properties, the optical response is strongly affected by the surface morphology such as surface roughness [38], periodic structures, texturing. Even if two surfaces have identical texture and geometry, their optical response can differ significantly depending on the material. This is especially important when analyzing the intensity of the reflected or scattered light. While the overall scattering pattern may remain similar, the total intensity can change due to

material-specific optical constants. As a result, the detected optical signal is shaped by both the material’s properties and the surface's microstructure [39].

Since a fixed wavelength and a single material type was used in this study, the detected optical signal can be shaped only by surface’s microstructure in this work.

Although transmission is included in the theoretical formulation of optical interaction, it was not measured in this study. Therefore, the focus remains on reflected and scattered components [40].

2.2 Scattering Theory Fundamentals

Scattering behaviors can be considered in different categories by the relationship between the characteristic size (d) of the surface features and the wavelength of the incident beam (λ). These classifications provide a framework for understanding how light interacts with surfaces that have different structural complexities and feature sizes [41].

2.2.1 Rayleigh, Mie and Geometric Scattering

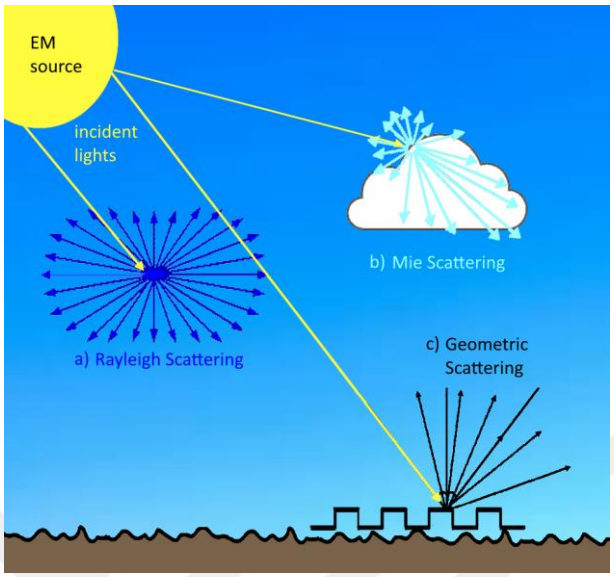

Figure 2.1 Schematic representation of (a) Rayleigh scattering, (b) Mie scattering, and (c) geometric scattering under electromagnetic illumination. Although the light source is represented symbolically, the incident wave in this study corresponds to a monochromatic laser beam ($\lambda = 650$ nm).

When the wavelength of the light is much larger than the characteristic size of the surface, scattering is expected to occur proportionally in all directions, as seen in Figure 2.1a). This phenomenon is known as Rayleigh scattering [9], [42]. Blue appearance of the sky is the result of the preferential scattering of shorter wavelengths by atmospheric molecules. Similarly, the reddish color of sunsets occurs because blue light is scattered away over the longer path through the atmosphere. In optical systems, if the surface roughness is not at atomic levels at optical surfaces, Rayleigh scattering is typically negligible and does not significantly impact scattering measurements.

Mie theory is relevant for situations where the characteristic size and the wavelength of the laser are comparable. In this regime, scattering highly depends on angle and becomes more difficult to examine [43] since it's mostly anisotropic, as shown in

Figure 2.1b). Mie scattering plays a significant role in systems containing spherical or cylindrical particles. A common real-world example of Mie scattering [44] is the whiteness of clouds or milk, which results from the scattering of all visible wavelengths by water droplets or fat globules similar in size to the light wavelength. It is commonly observed in systems such as colloidal suspensions, biological tissues and microstructures. In such cases, the angular distribution and intensity of scattered light vary significantly based on the refractive index and size of the scattering elements.

If the characteristic size is much larger than the wavelength of the laser, the scattering pattern follows the principles of geometric optics. In this type of scattering, strong and well-defined scattering patterns arise from reflection [45], refraction, and diffraction as illustrated in Figure 2.1c). Diffraction effects greatly affect the scattering on periodic micro surfaces such as diffraction gratings and photonic crystals. One everyday example of this phenomenon is the rainbow-like patterns observed on the surface of a CD, where the regularly spaced grooves act as a diffraction grating. The angular distribution of the scattered light is highly affected by the periodic arrangement of these structures, allowing precise analysis of surface properties [46].

While the comparison between the characteristic size and the wavelength gives a qualitative understanding of the scattering regime, the dimensionless size parameter provides a more complete description, as it incorporates the wave number $k = 2\pi/\lambda$ and shows the phase-based interaction of the incident wave with the structure. Hence, relation and classification can be expressed as in Eq (2.5) [47]

$$x = \frac{2\pi d}{\lambda} \tag{2.5}$$

The value of x determines the dominant scattering regime. x represents the dimensionless size parameter, d represents the characteristic size, and λ is the wavelength of the incoming light.

If $x \ll 1$, Rayleigh scattering is the appropriate model.

If $x \approx 1$, Mie scattering is the appropriate model.

If $x \gg 1$, geometric scattering is the appropriate model.

For the periodic micro-structured surfaces investigated in this study, the appropriate scattering model falls within the geometric scattering regime. This is supported both by the size parameter x >> 1 and the observation of clear diffraction orders in the angular scattering distribution.

2.2.2 Near-Field and Far-Field Scattering

Based on the distance from the scattering surface, scattering behaviors can be examined in two regions which are near-field and far-field.

Near-field region is very close to the scattering surfaces like a few wavelengths. Figure 2.2 demonstrate that EM fields are very complex in near-field regions and strong field interactions can occur in near-field regions. Also, evanescent waves do not propagate into free space, but they are strongly bound to the interface which makes the measurements very difficult in that area. Near-field effects are significant in high-resolution imaging techniques or when surface plasmon interactions are involved.

The far-field region refers to the area where the distance from the scattering surface is much larger than the wavelength of the incident light. In this region, EM fields become simpler and can be approximated as plane waves [48]. The angular distribution of the scattered light becomes stable, which allows accurate and repeatable measurements. Since the phase relationships between scattered waves are well-defined in the far-field, as illustrated in Figure 2.2, interference and diffraction patterns can clearly emerge. Unlike the near field region, there are no evanescent waves, and the scattered energy propagates freely into space. Most optical detectors are designed to operate in the far-field, making this region suitable for angle-resolved scattering measurements and diffraction analysis [49].

Since near-field measurements are not feasible for angle-dependent detection, they are not relevant to the experimental method used in this study. Therefore, all measurements in this study were carried out in the far-field region, where the distance from the surface is much larger than the wavelength of the incident light.

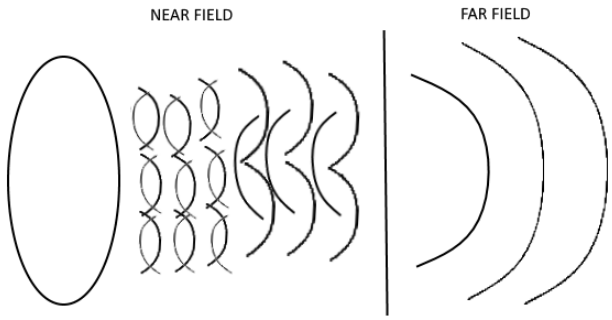

Figure 2.2 Near Field and Far Field Regions

2.3 Diffraction Theory from Periodic Structures

Electromagnetic waves interacting with periodic surfaces produce diffraction when the structural spacing matches the order of the wavelength. The regularly spaced features cause constructive and destructive interference of scattered light, resulting in discrete angular directions called diffraction orders [50]. These orders provide direct information about the surface periodicity, especially in the far-field region. Diffraction-based analysis is widely used to investigate micro- and nano-patterned surfaces where conventional imaging methods are insufficient.

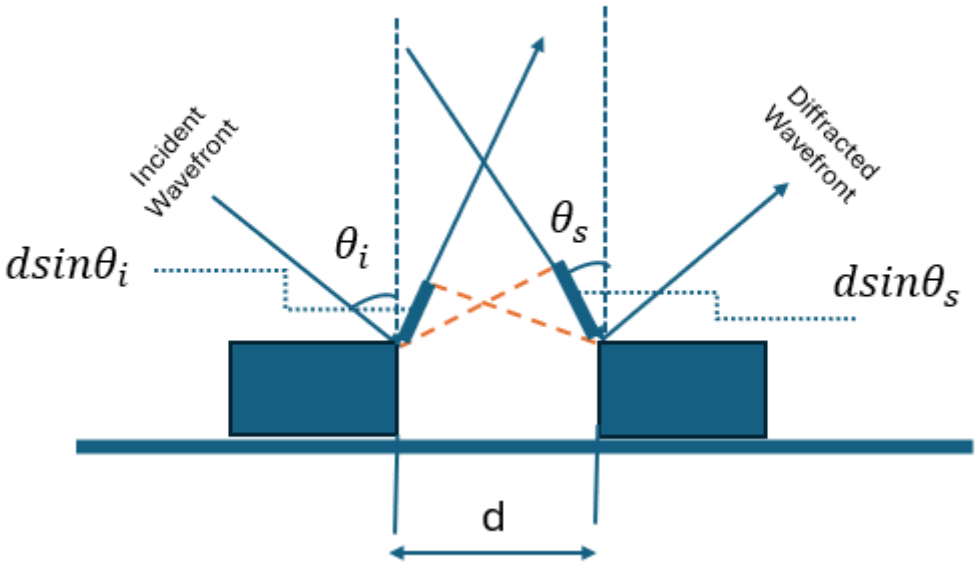

Figure 2.3 Diffraction from a Periodic Grating Surface Showing Multiple Diffraction Orders

When a beam of monochromatic light is incident on such a surface, the condition for constructive interference [51] is described by the grating equation (2.6):

$$d(sin\theta_i + sin\theta_m) = m\lambda \tag{2.6}$$

Here, d is the grating period, θ_i is the angle of incidence, θ_m is the angle of the m^{th} diffraction order relative to grating normal, λ is the wavelength of the incident light,

and m is the diffraction order. The angular positions of diffracted beams, the surface periodicity and the wavelength can be examined with the equation (2.6).

Each diffraction order corresponds to a specific angle where the scattered light intensity peaks. The orders can take positive, negative or zero values. Positive orders occur on one side of the specular reflection [52], while negative orders appear symmetrically on the opposite side. The zero order corresponds to specular reflection. Measuring the angles of these diffraction orders relative to the grating normal allows the surface periodicity to be calculated for a given wavelength using equation (2.6).

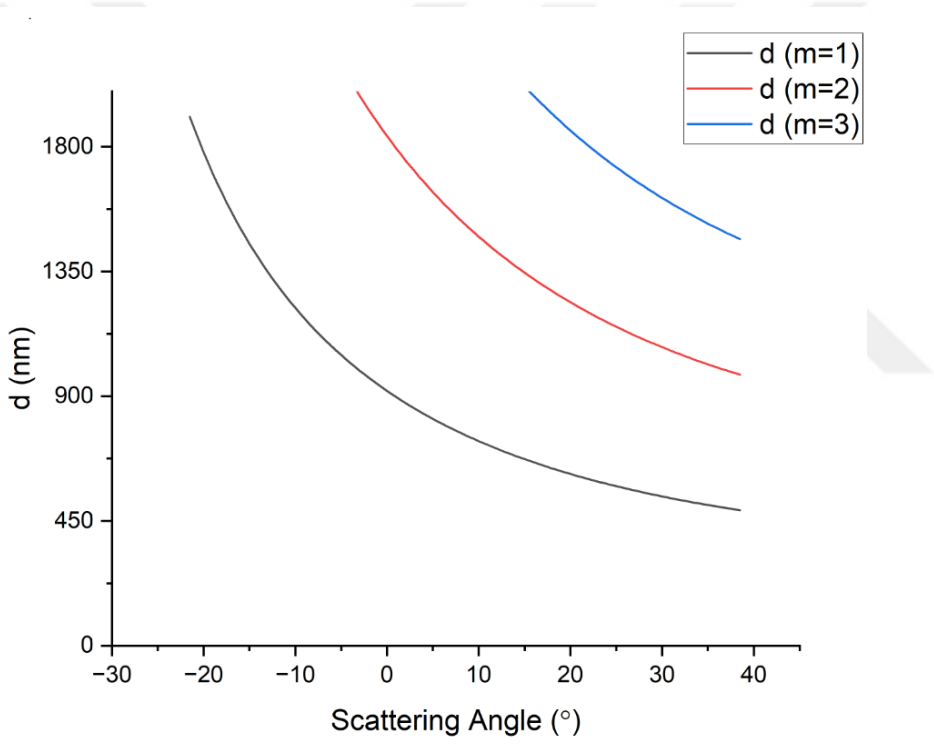

Figure 2.4 Calculated Surface Periods vs. Diffraction Angle for $\theta_i = 45°$, $\lambda = 650$ nm

The Figure 2.4 demonstrate how the diffraction angle changes depending on the surface periodicity for a fixed wavelength and incident angle. As the grating period d increases, the diffraction angle for a given order shifts closer to the specular beam direction. This model was created to provide a general estimation of surface

periodicities based on the angular position and direction of the diffraction order relative to the specular reflection [53].

In the constructed model, it was observed that although the distance between the periodic features (shown in red, green, and turquoise) increases by 500 nm, the diffraction angle relative to the grating normal increases more significantly. This increases the angular distance between the orders, which makes it easier to distinguish them. For small-period structures, diffraction occurs at lower angles, and it becomes important to have high angular resolution to distinguish closely spaced peaks. On the other hand, for larger periods, diffraction angles are higher and may approach the limits of the system's angular range, which requires a broader scanning window [53].

On some surfaces, certain diffraction orders may not appear or may be very weak. This can be related to the shape or symmetry of the surface pattern. For example, in blazed or non-sinusoidal gratings, some orders may be suppressed. These effects should be considered while analyzing the angular scattering data.

If the surface pattern is symmetric, the diffraction pattern is usually symmetric around the specular reflection. But if the left and right sides of the pattern look different, it may indicate surface defects, tilts, or non-uniform feature sizes.

2.4 Angle Resolved Scattering Method

ARS is an optical technique used to investigate the interaction of light with structured surfaces by examining the angular distribution of light scattered from the surface [18]. The intensity of the scattered light is measured as a function of the detection angle. The angular distribution often shows clear and important features such as specular reflection and diffraction peaks. These features are closely [54] related to the surface morphology and periodicity.

The working principle of ARS relies on the spatial separation of scattered light components due to interference effects that arise from surface features. Periodic

structures on the surface cause incident light to diffract at certain angles based on conservation of momentum. This relationship can also be examined mathematically with grating equations. The angular positions of the diffracting beams and the intensities of these beams relative to each other provide important information about the spatial frequency, symmetry and uniformity of the surface [55].

A standard ARS setup usually consists of a fixed incident beam, a stage where the sample can be centered, and a circular track that allows the photo detector to rotate around the sample, as seen in Figure 2.5. The incident light beam is adjusted to hit the surface between 0 and 90 degrees. The specular reflection angle serves as a reference point in the angular distribution, around which diffraction peaks may appear symmetrically or asymmetrically, depending on the surface structure [21].

Due to its straightforward operational principle and relatively simple equipment requirements, ARS enables indirect, non-contact characterization of patterned surfaces. The absence of surface preparation steps significantly reduces the overall measurement time which makes this technique fast and efficient.

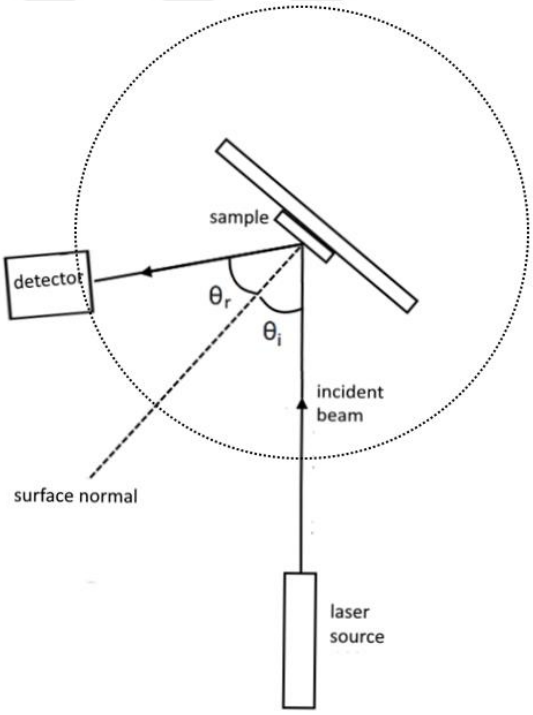

Figure 2.5 Angle Resolved Scattering Set Up Demonstration

CHAPTER 3

EXPERIMENTAL WORK

This chapter presents the experimental work conducted throughout the study. The first part focuses on the instrumentation setup, including the optical, mechanical, and electronic components of the custom-built ARS system as shown in Figure 3.1. Following this, the surface preparation process for the samples used in the measurements is described in detail.

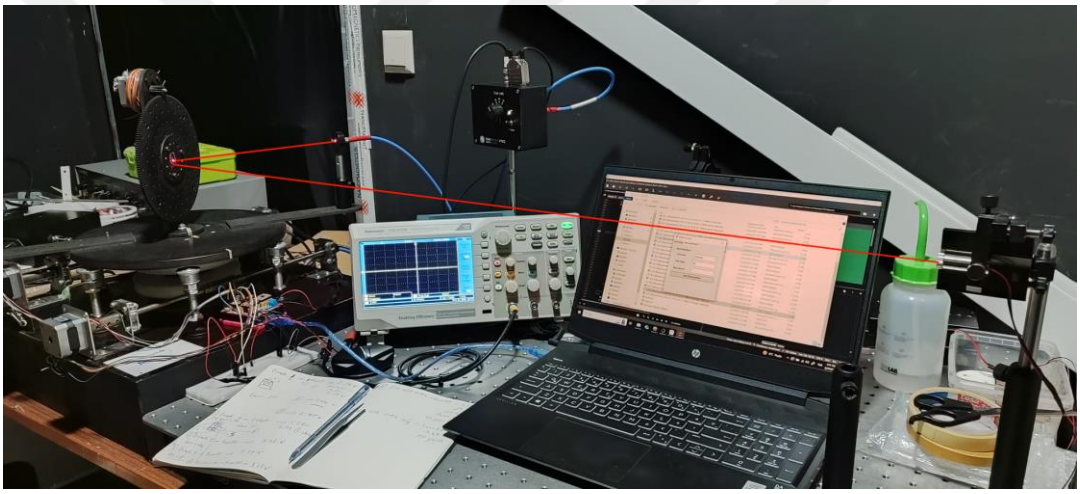

Figure 3.1 General view of the experimental ARS setup

3.1 Instrumentation of the ARS Measurement System

The experimental setup developed for angle-resolved scattering measurements is designed to accurately measure the angular distribution of scattered light from micro-structured surfaces. The X and Y rotational stages are supported by a rigid mechanical structure resting on six symmetrically positioned legs, each separated by 60° intervals, as shown in Figure 3.2. These legs contain precision ball bearings to

reduce friction and ensure highly accurate and smooth rotational movements along the X-axis, enhancing the overall angular measurement precision.

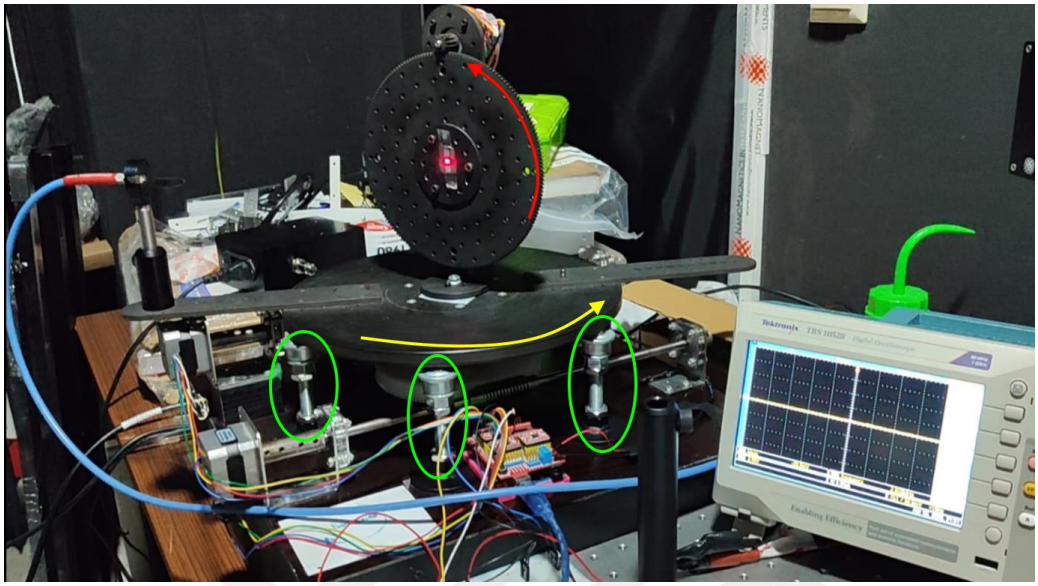

Figure 3.2 The yellow and red arrows show the rotation of X-axis and Y-axis. The green circles represent the legs spaced 60 degrees apart.

Two axes, X and Y, facilitate precise angular positioning. The X-axis, with a platform diameter of 30 cm, achieves a full 360° rotation in 115200 steps, resulting in an angular resolution of 0.003125° per step. The Y-axis, featuring an 18 cm diameter platform, completes 360° rotation in 28800 steps, thus providing an angular resolution of 0.0125° per step. These parameters are critical for accurate determination of scattering angles during measurements.

The optical subsystem consists of an s-polarized, 650 nm wavelength, 5 mW red laser. Ideally, a laser with a shorter wavelength would have been more suitable for resolving finer surface features due to its smaller diffraction-limited spot size. However, due to limitations in the laboratory environment and the availability of a 650 nm red laser, this configuration was adopted. Despite its relatively longer wavelength, the red laser still offers sufficient sensitivity for capturing angular

scattering patterns from micro-structured surfaces, as also demonstrated by Sterligov et al. using 632.8 nm light in elastic scattering measurements [56]. The laser beam is aligned using precision optical mounts to ensure consistent illumination of the sample surface, placed at a fixed distance of 100 cm from the laser source. Scattered light from the surface is collected by a QP400-2-VIS-NIR optical fiber with a core diameter of 400 µm positioned 24 cm from the sample, and is subsequently coupled directly into a photodetector.

Two separate custom electronic circuits were designed for the system: one for controlling the laser and the other for processing the photodetector signal. The laser driver circuit includes a potentiometer and a diode protection component to ensure stable and safe laser operation with adjustable power output as shown in Figure 3.3.

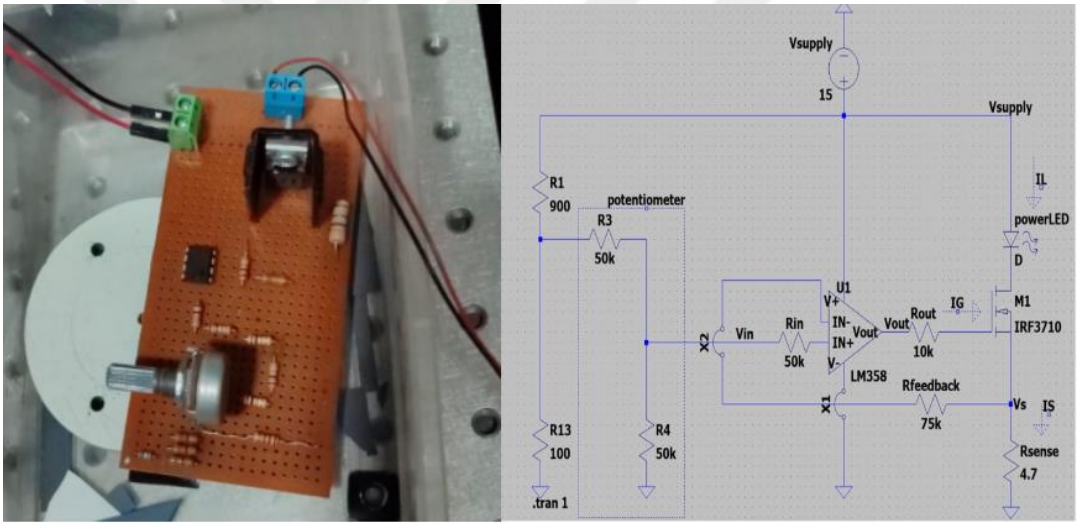

Figure 3.3 Circuit and implementation of laser power control unit. Left: breadboard implementation; Right: schematic of the circuit.

The photodetector initially provided a gain adjustable from 0 to 70 dB; however, by integrating an additional operational amplifier, the gain range was effectively extended up to 90 dB. Furthermore, this operational amplifier circuit converts the negative voltage outputs from the photodiode into positive voltages, compatible with

the 0–5 V range of the Arduino's analog-to-digital converter (ADC). Real-time monitoring of the photo detector output was consistently conducted using an oscilloscope, ensuring accurate measurements and verifying the reliability of the electronic subsystem.

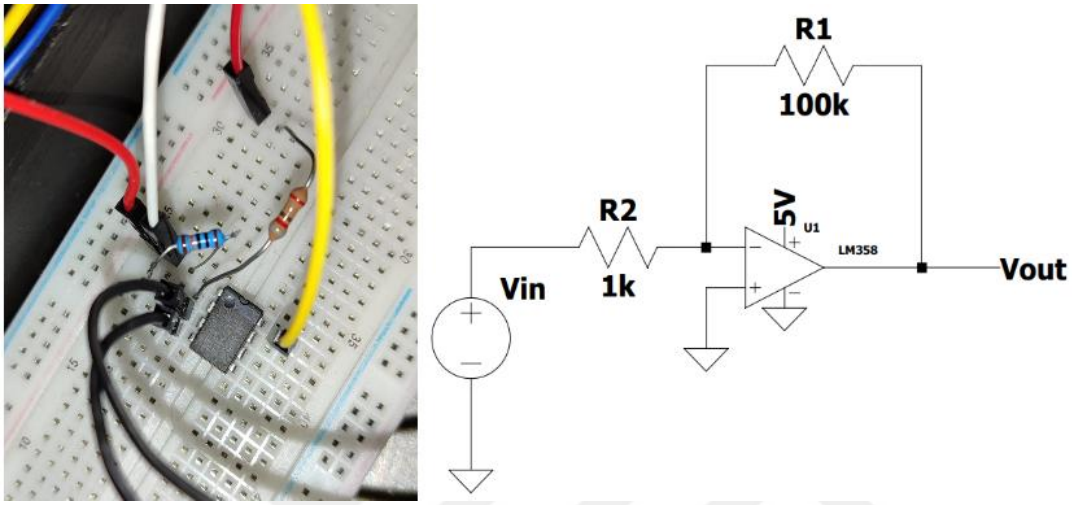

Figure 3.4 Signal conditioning circuit used for inverting and amplifying the photodetector output. Left: breadboard implementation; Right: schematic of the LM358-based inverting amplifier.

Table 3.1 Variation of input and amplified voltages at different gain levels for specular reflection.

Gain (dB)	0	10	20	30	40	50	60	70
$V_i(V)$	0.01	0.01	0.02	0.09	0.030	0.098	0.30	0.99
$V_s(V)$	0.009	0.17	0.42	1.25	3.67	3.67	3.67	3.68

Table 3.1 presents the initial voltage values V_i of the light reflected from the specular direction of a sample, and the corresponding amplified voltages V_s after passing through the gain circuit for different gain values. While the increase in gain leads to

signal saturation around the specular region, it enables the detection of diffraction orders on periodic surfaces and the observation of diffusely scattered light on rough surfaces, thereby allowing surface morphology to be interpreted. During scans near the specular direction, using lower gain values is preferable to avoid saturation, whereas at higher scattering angles, increased gain enhances measurement sensitivity.

Control and data acquisition processes are managed by an Arduino microcontroller interfaced with a custom-developed Python software platform. This software allows precise and automated control of the stepper motors, facilitating accurate angular positioning of both axes in clockwise and counterclockwise directions. Additionally, it enables real-time acquisition and systematic storage of voltage data from the photodetector, forming a comprehensive dataset for subsequent analysis.

This integrated experimental setup, combining advanced mechanical design, precise optical alignment, sophisticated electronic circuitry, and automated software control, ensures robust, accurate, and repeatable ARS measurements necessary for detailed optical characterization of micro-structured surfaces.

3.2 Sample Preparation

Two distinct groups of micro-structured silicon samples were used in this study: Group A with periodic surface patterns and Group B with rough, non-periodic textures. Each group was fabricated using different processing methods suited to their intended structural characteristics.

3.2.1 Periodic Surface Structures

Group A samples were fabricated using Laser-Induced Periodic Surface Structuring (LIPSS) on 525 μm thick p-type silicon wafers. A homemade femtosecond laser

system with a central wavelength of 1032 nm and a repetition rate of 1 MHz was used for texturing the surface. Periodic microstructures were produced over areas of 5 mm x 5mm and 3 mm x 3mm. Six different samples were prepared by varying the scanning speed and hatch distance to achieve different surface profiles as shown in Table 3.2. The fabrication procedure is described in more detail elsewhere [57], [58]

Table 3.2 Laser processing parameters for Group A samples

Sample Number	Laser Speed (m/s)	Hatch Distance (μm)
A1	5	4
A2	7	4
A3	10	4
A4	10	7
A5	5	1
A6	10	1

3.2.2 Rough Surface Structures

Group B samples feature non-periodic, rough surface textures produced by a two-step fabrication process involving chemical etching followed by laser exposure. First, n-type silicon substrates were immersed in a mixture containing 15 mL of deionized (DI) water, 60 mL of hydrofluoric acid (HF), and 35 mL of hydrogen peroxide (H_2O_2). The samples were irradiated with a high-power laser under different power and duration conditions. Power loss was estimated as 20%, and the output intensity (I) was calculated accordingly. The parameters for each sample are shown in Table 3.3. Further details of the fabrication procedure can be found in [59], [60].

Table 3.3 Photochemical treatment parameters of Group B samples

Sample Number	Laser Power (W)	Duration (min)	Estimated Output Power (W)	Irradiated Area (cm^2)	Intensity I (W/cm^2)
B1	1.5	60	1.2	π	0.38
B2	2.0	60	1.6	π	0.51
B3	2.5	60	2.0	π	0.64

CHAPTER 4

DISCUSSION

The primary aim of this study was to determine whether microstructured surface features could be characterized through their optical scattering behavior, using a custom-designed angle resolved scattering system. To this end, a series of silicon surfaces fabricated by laser texturing were analyzed with the goal of extracting information related to structural periodicity, surface uniformity, and microscale roughness. In contrast to conventional imaging techniques, this method offers a non-contact, fast, and scalable alternative for surface evaluation, and is particularly suited for detecting optical signatures that correlate with subtle morphological differences.

In this chapter, three complementary analyses are performed on the angular scattering data. 4.1 Surface Uniformity and Small-Angle Scattering Behavior focuses on surface uniformity by comparing five-point scattering measurements across each sample, emphasizing the stability and symmetry of the specular region. 4.2 Diffraction Orders and Periodicity addresses diffraction order analysis, where angular peak positions are used to identify periodic structures and estimate surface period via the grating equation. Finally, 4.3 Surface Roughness and Angle-Resolved Scattering Behavior examines roughness characteristics based on diffuse scattering behavior and wide-angle profiles, incorporating statistical indicators and comparisons with AFM and SEM observations.

In all cases, the intensity data were smoothed using Savitzky–Golay filtering to reduce noise while preserving the original shape of the scattering profiles. This filtering technique was selected for its ability to retain peak height and width, which are essential for resolving key angular features [61]. The combined outcome of these

analyses serves to evaluate how reliably angle resolved scattering can capture variations in surface texture and validate its performance against standard morphological tools.

4.1 Surface Uniformity and Small-Angle Scattering Behavior

To evaluate surface uniformity, each angular profile was analyzed in terms of several optical parameters: the full width at half maximum (FWHM), the sharpness and symmetry of the main peak, background intensity levels, and the presence of extended tails around the specular region. These features are particularly sensitive to local surface variations and provide a detailed basis for assessing spatial consistency.

In order to probe these effects across the surface, angle-resolved scattering profiles were measured from five different positions (middle, top, bottom, left, and right) on each sample from Group A, as shown in Figure 4.1, to assess whether angular scattering behavior remains consistent across the structured surface.

Samples A1 to A3 were chosen for this analysis since they share the same hatch distance of 4 μm but differ in laser scanning speeds, 5, 7 and 10 m/s respectively. This allows for the evaluation of how scan speed influences spatial uniformity under otherwise identical fabrication conditions.

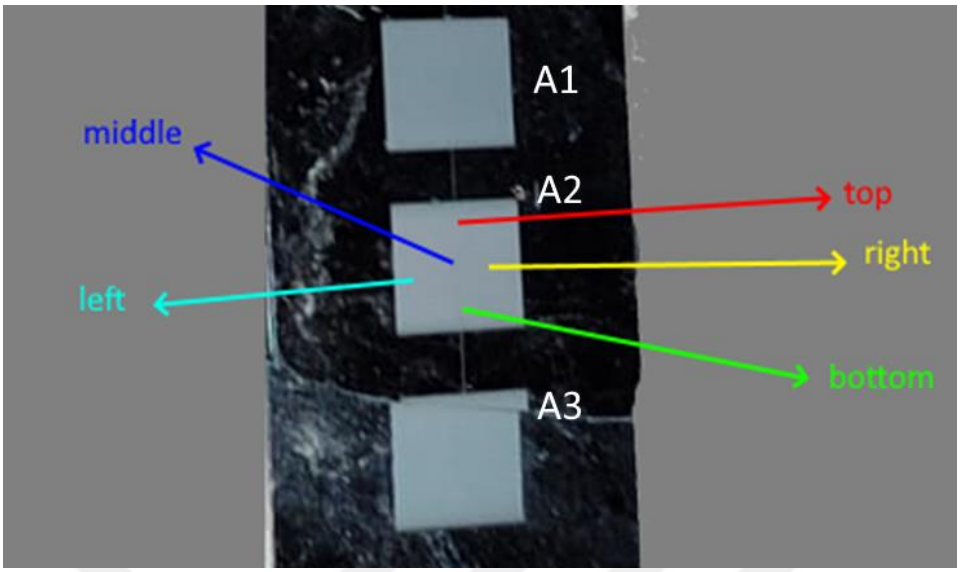

Figure 4.1 Measurement locations on A1, A2 and A3 samples for uniformity analysis. ARS data were collected at top (T), bottom (B), middle (M), left (L), and right (R).

In contrast, Group B samples were fabricated using a photochemical process, resulting in etched regions located at varying positions across each sample, often separated by unetched areas. Therefore, while Group A followed a fixed five-point pattern, Group B measurements were taken from as many distinct etched areas as possible to ensure representative sampling of the surface texture as illustrated in Figure 4.2.

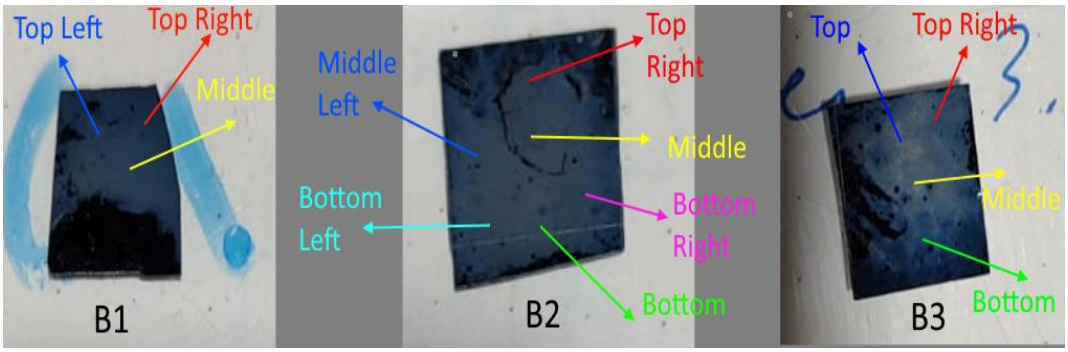

Figure 4.2 Measurement locations on Group B samples. ARS data were collected from different locations.

For consistency in analysis, the angular axis was redefined such that the specular reflection, corresponding to the incident angle of 45°, is assigned to $\theta = 0°$. During measurements, the detector was first aligned to the specular direction, then moved 500 steps clockwise and scanned over 1000 steps back toward the incident angle. This scanning procedure allowed a symmetric angular range of ±1.5° around the specular reflection to be recorded for each measurement.

All profiles were normalized to their respective maximum values to facilitate comparison across different regions without being affected by absolute intensity fluctuations due to minor alignment differences or surface contamination. Since the goal is to assess spatial consistency in scattering behavior, this narrower angular range was deemed sufficient.

4.1.1 Group A (Periodic Structured Samples)

4.1.1.1 A1 Sample (Laser Speed: 5 m/s, Hatch Distance: 4 µm)

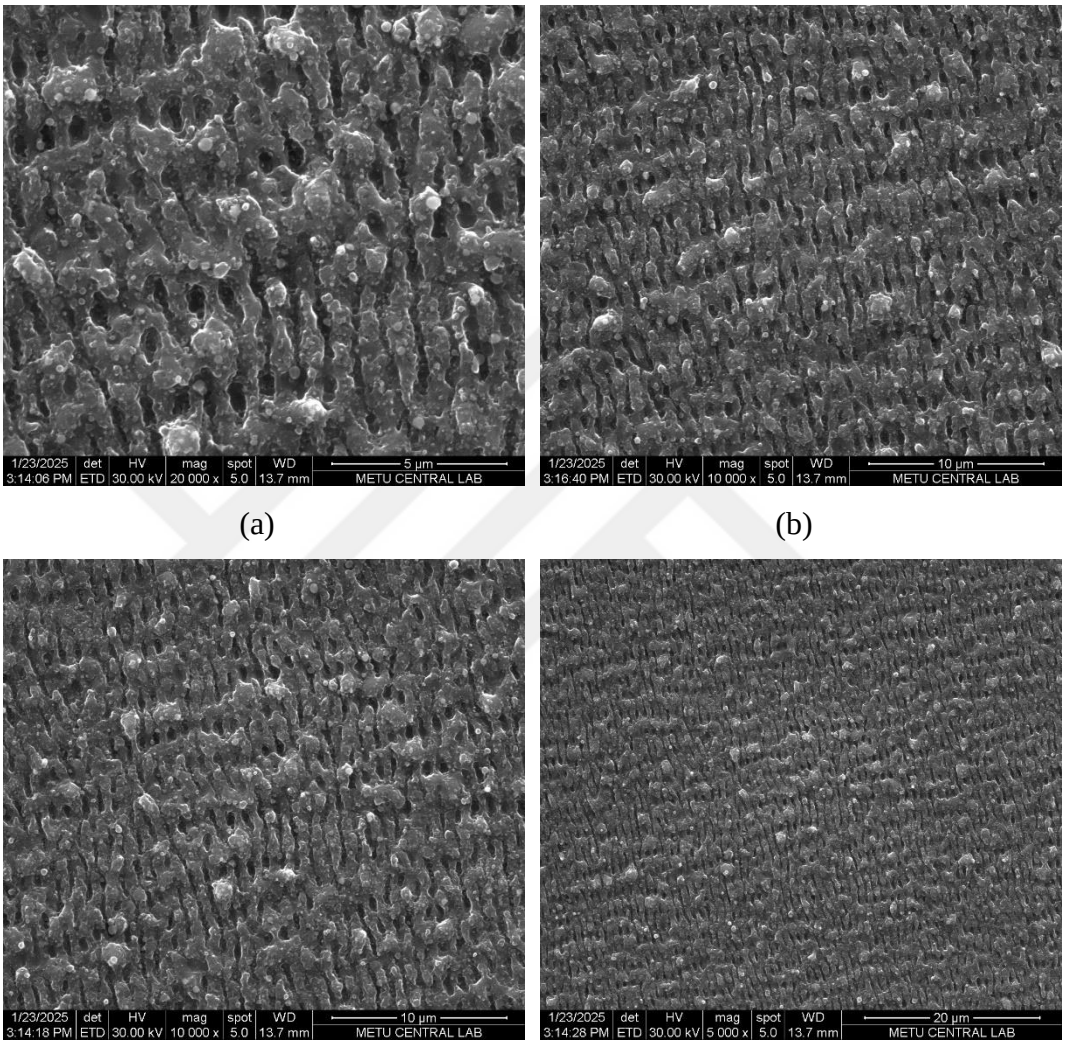

Figure 4.3 Surface morphology of the A1 sample fabricated using LIPSS with a laser speed of 5 m/s and a hatch distance of 4 µm. SEM images were taken from different regions at different magnifications: (a) 20000× (scale bar: 5 µm), (b) 10000× (scale bar: 10 µm), (c) 10000× (scale bar: 10 µm) and (d) 5 000× (scale bar: 20 µm)

Figure 4.3 presents SEM images of the A1 sample fabricated using LIPSS at a laser speed of 5 m/s and a hatch distance of 4 μm, captured from different regions at varying magnifications. At higher magnification (Figure 4.3a), the surface exhibits clearly defined submicron-scale ridges with good periodicity. Some localized defects such as minor groove interruptions or shape distortions are visible, but these remain isolated and do not significantly affect the overall structure. As the magnification decreases (Figure 4.3 b-d), the periodic texture becomes more pronounced and uniformly aligned, suggesting that the surface features are consistently reproduced across the sample. The observed morphology indicates that the chosen laser parameters were effective in producing uniform periodic features, supporting reliable and consistent scattering outcomes.

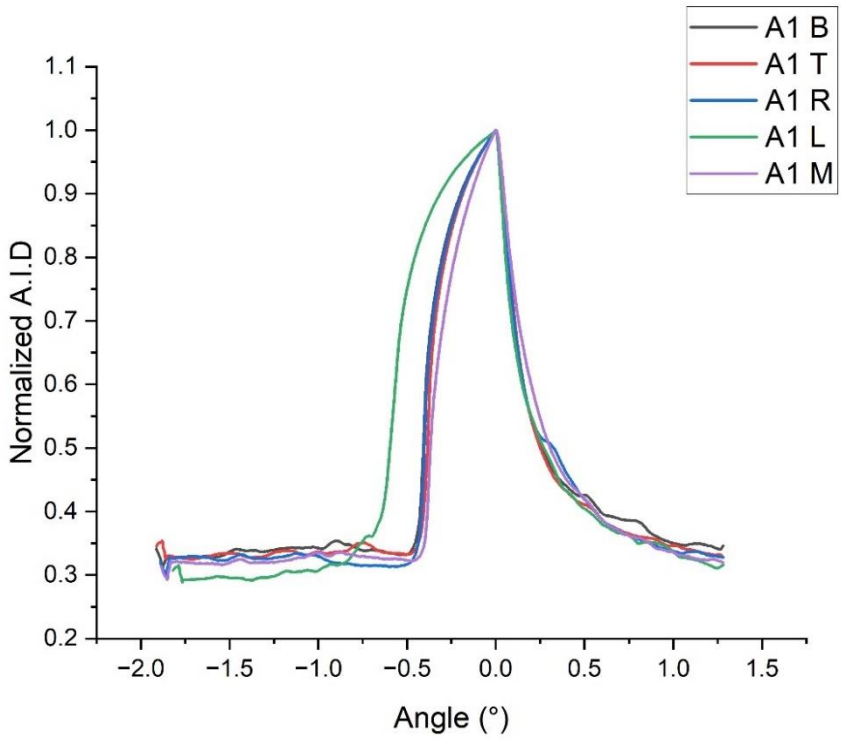

Figure 4.4 Angle-resolved scattering intensity profiles measured at five different positions on the A1 sample surface: Top (T), Bottom (B), Left (L), Right (R), and Middle (M).

To evaluate the angular uniformity of the A1 sample, scattering measurements were collected from five surface positions. All measurements are normalized to their respective maximum values, and the resulting profiles are presented in Figure 4.4. Due to minor mechanical deviations during motorized scanning, the angular positions of the specular peaks varied slightly between measurements. To enable meaningful comparison, each curve was laterally shifted so that their specular peaks align at 0°, ensuring a consistent reference point across all regions.

The angular scattering profiles obtained from the top, bottom, middle, and right positions exhibit strong overlap in both shape and width, each showing a well-defined specular peak and comparable intensity distributions. This indicates a high

level of consistency in scattering behavior across these regions. The SEM images shown in Figure 4.3a–d were captured from different locations on the sample surface, and all display similar periodic structures with consistent orientation and spacing. While these images do not represent the entire surface, their similarity supports the presence of regularly formed features across multiple regions. When considered together with the angular scattering results, these localized observations suggest that the periodic texture seen in the SEM images is likely representative of a broader uniformity over the sample area covered by the measurements.

The A1 L position in Figure 4.4, however, exhibits a broader and more rounded specular peak. Since all curves were aligned at 0°, this broadening reflects an increased full width at half maximum (FWHM), rather than a shift in peak position. Several structural factors may contribute to this broadening. The broader and more rounded peak observed at the A1 L position may result from several localized surface effects. A slight tilt in that region could cause the reflected light to spread over a wider angular range, increasing the apparent FWHM. Similarly, small variations in groove depth or ridge shape might weaken the constructive interference typically responsible for sharp peak formation, leading to a smoother profile. In addition, minor misalignments in the orientation of surface micro-facets can introduce angular dispersion, further broadening the scattering response. While these effects cannot be confirmed solely from the scattering data, they are plausible explanations consistent with the observed peak shape.

Despite the broader peak observed at the A1 L position, the general peak structure and the intensity distribution beyond ±1° remain comparable to the other measurements. Minor differences observed in the off-specular regions, such as small fluctuations or extended scattering tails, are consistent with localized morphological variations visible in the SEM images. These results demonstrate that the angular scattering response is largely repeatable across the sample, indicating a high degree of surface uniformity.

4.1.1.2 A2 Sample (Laser Speed: 7 m/s, Hatch Distance: 4 µm)

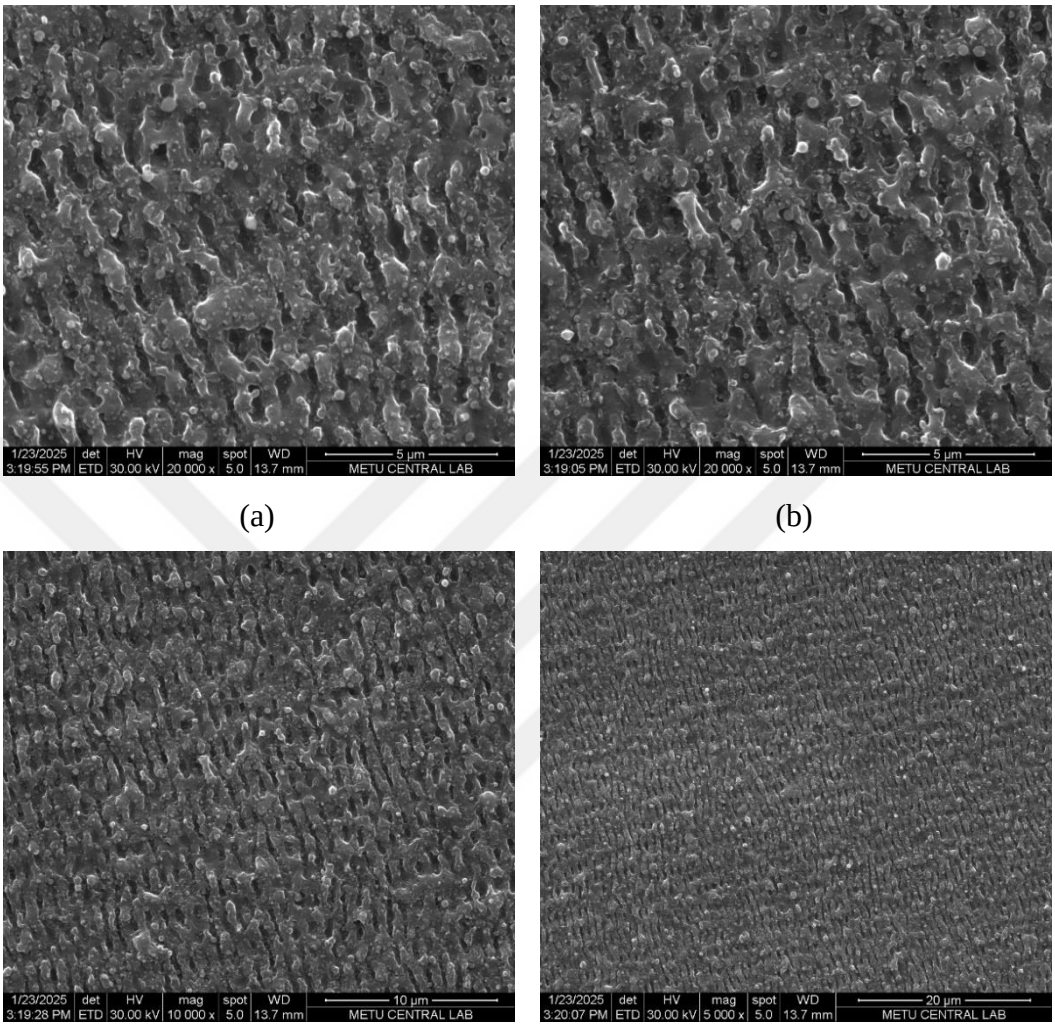

Figure 4.5 Surface morphology of the A2 sample fabricated using LIPSS with a laser speed of 7 m/s and a hatch distance of 4 µm. SEM images were taken from different regions at different magnifications: (a) 20000× (scale bar: 5 µm), (b) 20000× (scale bar: 5 µm), (c) 10000× (scale bar: 10 µm), and (d) 5000× (scale bar: 20 µm).

Figure 4.5 presents SEM images of the A2 sample fabricated using LIPSS with a laser speed of 7 m/s and a hatch distance of 4 µm, captured from different regions at

varying magnifications. At the highest magnification (Figure 4.5a–b), the surface reveals periodic ridge structures with submicron-scale spacing. Compared to A1, these ridges appear slightly less sharply defined and exhibit more frequent interruptions or local distortions. This may be attributed to the increased scanning speed, which reduces the laser-material interaction time, potentially limiting the energy delivery per unit area and reducing structural precision.

As the magnification decreases (Figure 4.5c–d), the overall surface texture maintains a quasi-periodic pattern, though local variations in ridge continuity and alignment become more apparent. These features suggest that while the fabrication parameters are sufficient to generate large-scale ordering, finer structural consistency may be affected by dynamic laser-material interactions at higher writing speeds.[41]

Nonetheless, the persistence of periodic features across different magnifications and regions suggests that LIPSS formation on the A2 sample was generally successful, with an acceptable degree of spatial uniformity.

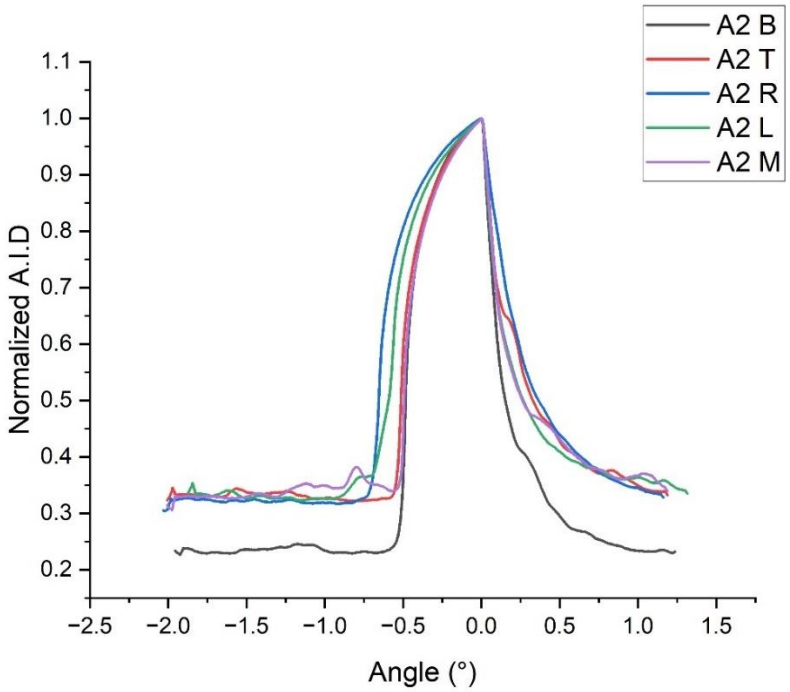

Figure 4.6 Angle-resolved scattering intensity profiles measured at five different positions on the A2 sample surface: Top (T), Bottom (B), Left (L), Right (R), and Middle (M).

Figure 4.6 shows the angle-resolved scattering intensity profiles measured from five different regions of the A2 sample. All measurements are normalized to their respective maximum values and laterally aligned to center the specular peak at 0°, compensating for minor mechanical deviations during motorized scanning.

The scattering profiles from the Top, Right, Left, and Middle regions exhibit strong agreement, featuring similar peak widths, heights, and angular slopes. This overlap suggests that the periodic surface structure is largely consistent and well-aligned across those areas. SEM images (Figure 4.5a–c) show continuous periodic patterns with only minor structural inconsistencies.

The A2 B region shows reduced peak intensity accompanied by elevated background scattering beyond ±1°, and a slightly narrower peak profile relative to the other positions. This suggests that the surface in this region may exhibit lower overall reflectance due to structural or optical variations, rather than a complete loss of periodic alignment. Such intensity reduction may stem from subtle surface defects, non-uniform laser exposure, or localized contamination. Notably, the reduced intensity in this region was consistently observed across multiple independent measurements. This observation is further supported by the diffraction-based analysis presented in Section 4.2.

Overall, the A2 sample demonstrates strong angular uniformity, with the A2 B region representing a localized deviation in optical response, potentially involving both reflectivity and structural variations.

4.1.1.3 A3 Sample (Laser Speed: 10 m/s, Hatch Distance: 4 µm)

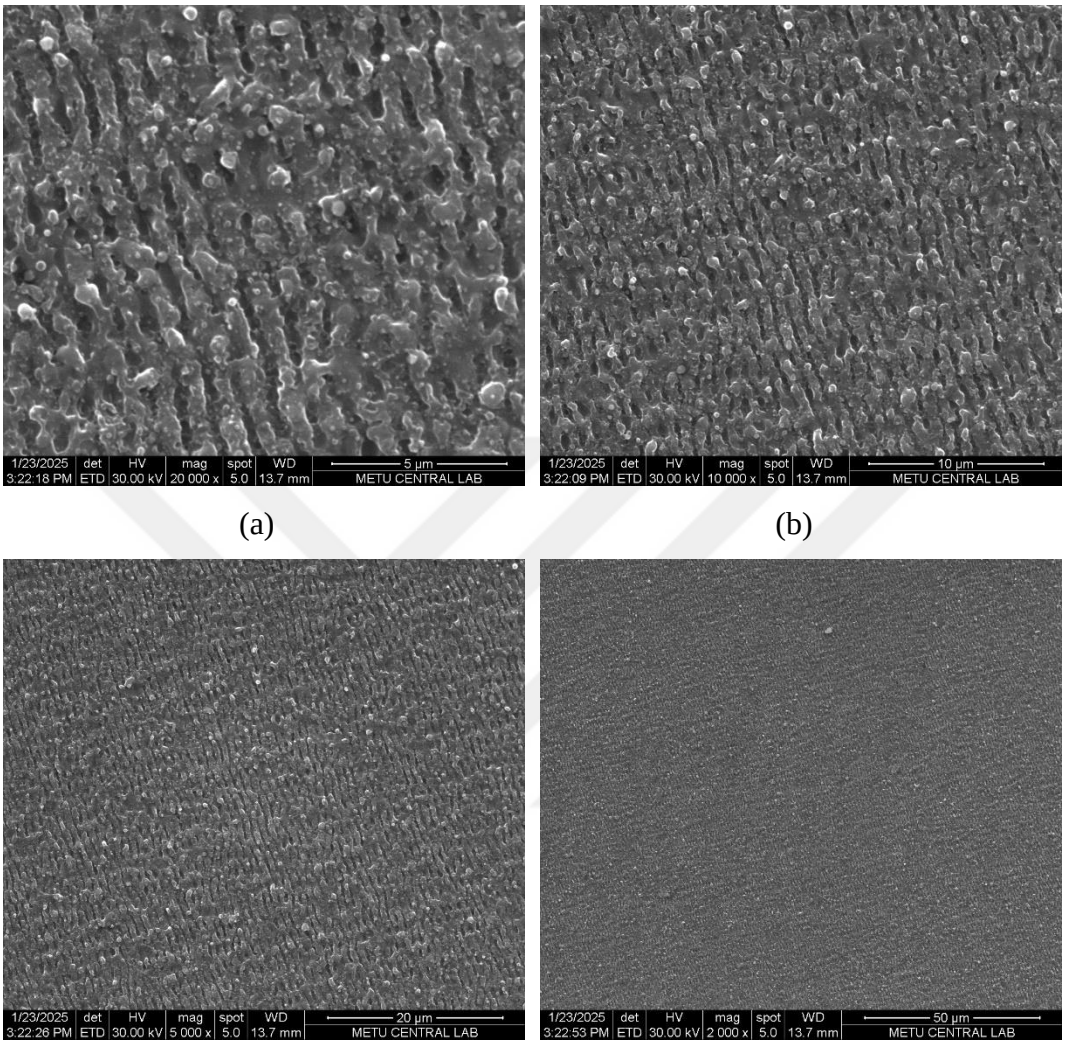

(a) (b)

(c) (d)

Figure 4.7 Surface morphology of the A3 sample, fabricated using a laser speed of 10 m/s and a hatch distance of 4 µm. SEM images were captured at four different magnifications: (a) 20000× (scale bar: 5 µm), (b) 10000× (scale bar: 10 µm), (c) 5000× (scale bar: 20 µm), and (d) 2000× (scale bar: 50 µm).

Figure 4.7 presents SEM images of the A3 sample, fabricated using LIPSS with a laser speed of 10 m/s and a hatch distance of 4 μm. Images were captured from different surface locations at four magnification levels.

At the highest magnification (Figure 4.7a), periodic ridges with submicron spacing are visible, and although small disruptions are present, the general ridge alignment remains clear. In (Figure 4.7b-c), the periodic structure becomes more uniformly defined, showing regularly spaced lines with consistent orientation. The lowest magnification image (Figure 4.7d) reveals a highly ordered ripple pattern extending across a wide area, indicating long-range alignment.

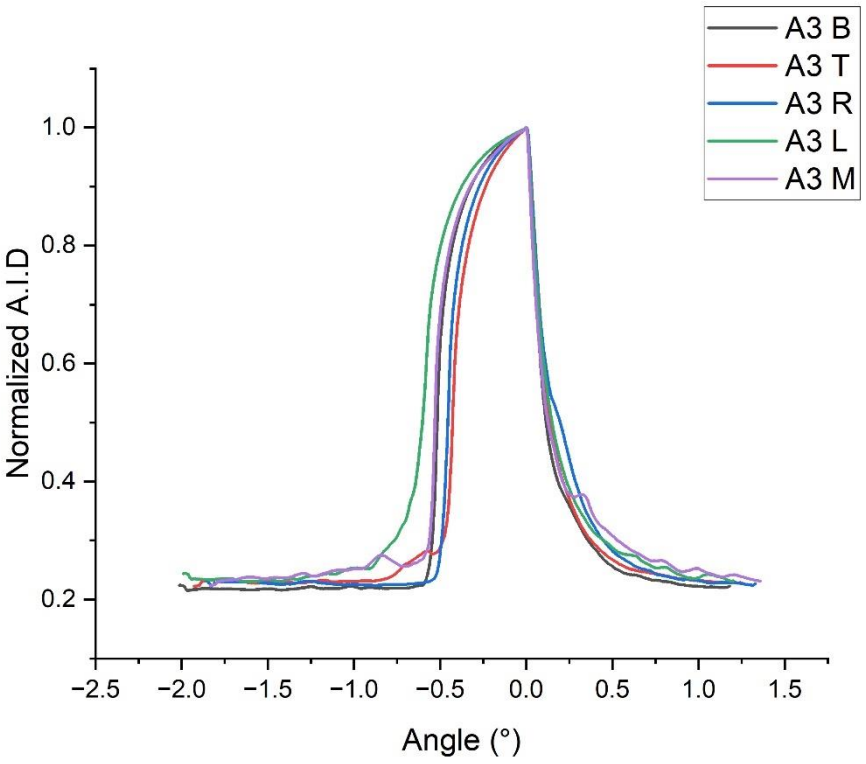

Figure 4.8 Angle-resolved scattering intensity profiles measured at five different positions on the A3 sample surface: Top (T), Bottom (B), Left (L), Right (R), and Middle (M).

Figure 4.8 shows angle-resolved scattering intensity profiles for the A3 sample, obtained from five distinct surface positions. All curves are normalized to their respective maximum values and aligned such that the specular peak positions coincide, enabling comparative evaluation of angular shape and intensity distribution.

The scattering curves exhibit remarkable overlaps across all positions, with nearly identical peak widths, heights, and angular slopes. This high level of agreement suggests that the surface periodicity is well-preserved and uniformly oriented across the sampled regions.

Compared to A1 and A2, the A3 sample shows the most consistent scattering response, with minimal variation in both the central peak and background regions. SEM images in Figure 4.7a-d, which were taken from different surface locations, also show uniform periodic features with clear alignment, further supporting the angular scattering results.

These findings indicate that the A3 sample demonstrates strong angular uniformity and a high degree of structural regularity, both locally and over extended regions. The combined SEM and ARS observations point to effective parameter tuning at the fabrication stage, particularly in achieving consistent orientation and pattern continuity.

4.1.1.4 Statistical Comparison of Group A

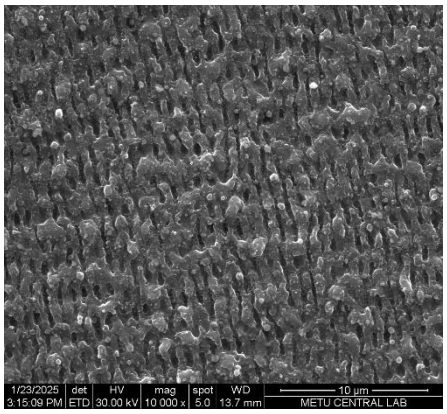

(a)

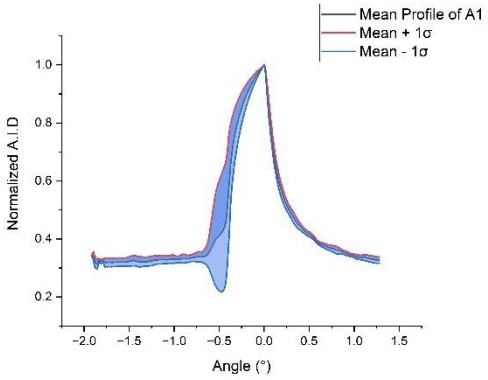

(d)

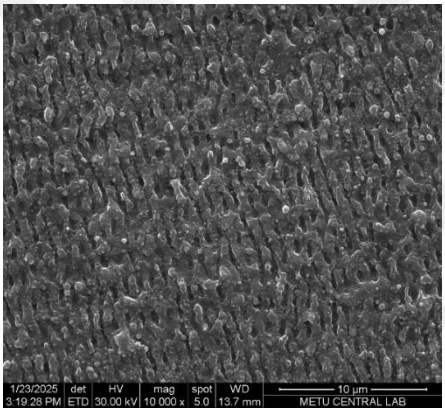

(b)

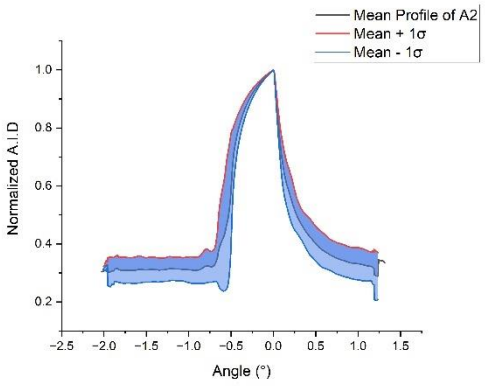

(e)

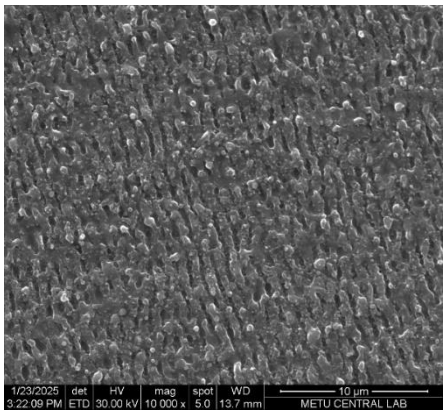

(c)

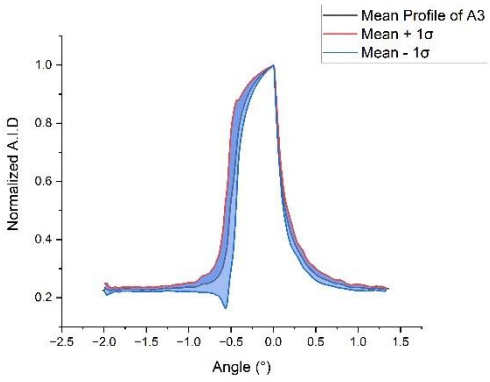

(f)

Figure 4.9 Statistical comparison of Group A samples using standard deviation profiles and representative SEM images. Left: SEM morphology at 10000× (scale bar: 10 μm). Right: Mean angle-resolved scattering profiles with ±1σ standard deviation.

Figure 4.9 presents the statistical comparison of the A1, A2, and A3 samples based on their average angular scattering profiles and corresponding standard deviation (STD) bands. The red curves represent the mean profiles obtained by averaging measurements from five distinct regions on each sample, while the shaded blue areas indicate ±1σ deviations at each angular point. The SEM images (Figure 4.9a–c) were selected at 10 μm scale to visually represent the overall surface morphology observed across different regions of each sample.

Among the three samples, A3 exhibits the most uniform angular scattering behavior, as indicated by the narrowest STD band and the sharply defined mean profile (Figure 4.9f). This result agrees with its SEM image (Figure 4.9c), which shows highly ordered, well-aligned ripples with minimal visible distortions. The small variation across regions suggests that the periodic structures are consistently formed over the sample area.

In contrast, A2 displays the largest standard deviation, particularly on the left side of the profile, as seen in Figure 4.9e. This elevated variation stems from the lower intensity observed in the region of A2 B, which contributes to a wider spread in the average data. The mean profile of A2 also appears slightly broader than those of A1 and A3, with a more gradual angular decay. This broader peak shape and higher variability correlate with the SEM image (Figure 4.9b), where periodic ridges are present but with more irregular spacing and alignment compared to A3.

The SEM image of the A1 sample (Figure 4.9a) shows periodic ripple structures with relatively uniform spacing and alignment. Although minor local distortions are present, they do not indicate widespread structural irregularity. In the corresponding

standard deviation profile (Figure 4.9d), the variation remains low across most angles, except for a slight increase in the negative angle region (e.g., -1° to -0.5°). This localized rise in scattering variation may be associated with the A1 L region, which exhibited a slightly different optical response, possibly, due to reduced reflection efficiency, surface contamination, or non-uniform laser-material interaction during fabrication. While SEM alone cannot confirm the source of this deviation, the consistency across other regions supports the overall structural uniformity of the A1 sample.

4.1.2 Group B (Etched Samples)

4.1.2.1 B1 Sample (1.5 W, 60 min)

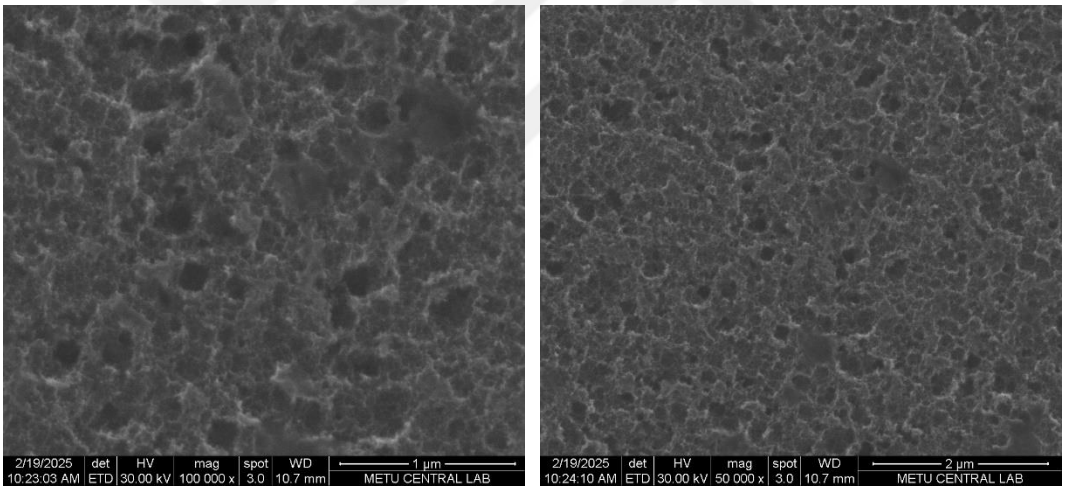

(a) (b)

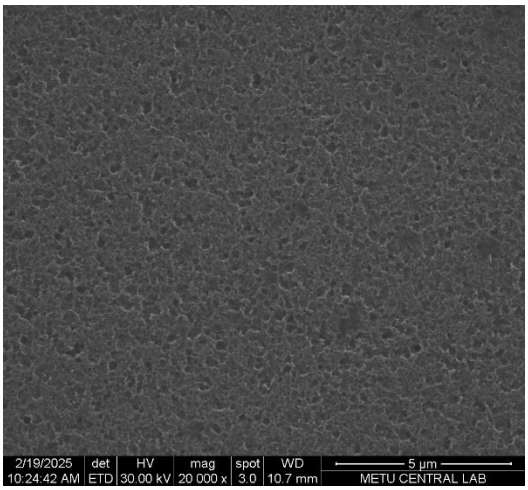

(c)

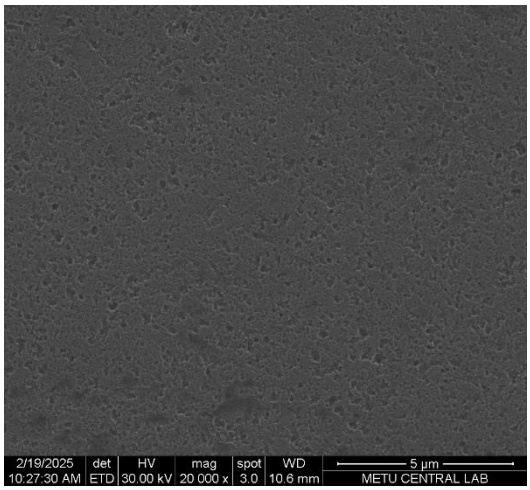

(d)

Figure 4.10 Surface morphology of the B1 sample irradiated for 60 minutes with a laser power of 1.5 W. The SEM images were taken from different regions at different magnifications: (a) 100000× (scale bar: 1 µm), (b) 50000× (scale bar: 2 µm), (c) 20000× (scale bar: 5 µm), and (d) 20000× (scale bar: 5 µm).

The SEM images presented in Figure 4.10 reveal the surface morphology of the B1 sample, which was fabricated through a two-step process involving chemical etching followed by laser irradiation at a power of 1.5 W for 60 minutes. The chemical treatment, conducted in a solution containing hydrofluoric acid, hydrogen peroxide, and deionized water, initially produced a disordered porous layer on the silicon surface. The subsequent laser exposure, applied with relatively low power, indicates that the laser treatment slightly altered the surface morphology, but did not induce significant smoothing, recrystallization, or large-scale reorganization.

At higher magnifications Figure 4.10a-b, the surface clearly exhibits nanoscale roughness characterized by irregular pores and depressions. These features are randomly distributed, lacking any periodic order, which is consistent with the non-directional nature of the chemical etching step. The laser's influence at this power level does not seem to fully suppress or reorganize these structures, but rather slightly enhances the contrast between elevated and recessed areas, possibly due to mild

surface melting or localized ablation. This is particularly evident in Figure 4.10a, where localized intensity variations suggest vertical depth modulation due to nanoscale topographical differences

At lower magnifications Figure 4.10c-d, the general uniformity of the roughness across a broader area becomes more apparent. There is no indication of large-scale restructuring or pattern formation, suggesting that the laser's energy was insufficient to induce macroscale effects.

Overall, the texture remains dominated by the chemical process, with the laser contributing only subtle morphological modifications. This supports the interpretation that surface intensity (~0.38 W/cm²) was below the threshold required for significant laser-induced patterning or periodic structuring.

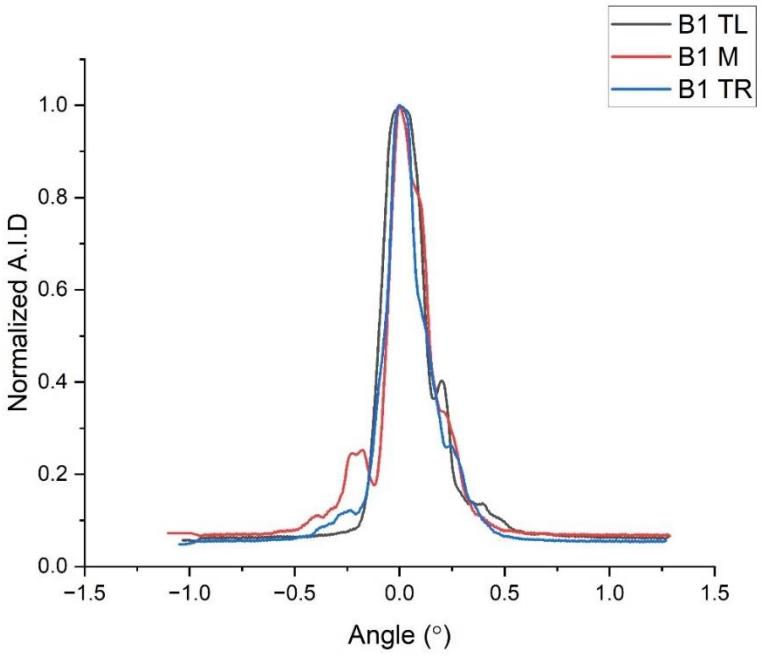

Figure 4.11 Normalized angle-resolved scattering intensity profiles measured at three different positions on the B1 sample surface: Top-Left (TL), Middle (M), and Top-Right (TR).

The angle-resolved scattering profiles measured from three distinct regions on the B1 sample surface (top-left, middle, and top-right) exhibit a strong specular peak centered at 0°, with relatively symmetric decay on both sides, as shown in Figure 4.11. To enable direct comparison, all profiles were normalized to their respective peak intensities and laterally shifted so that their peak positions aligned at 0°. The narrowness of the peak and the low background intensity away from the specular angle suggest that the surface features are predominantly sub-wavelength in scale, consistent with a rough, non-periodic morphology rather than an ordered structure.

While the general shape of the profiles is similar across the three positions, subtle differences are evident. B1 M displays a slightly broader shoulder on the left side of the peak, which may indicate localized variation in surface roughness or minor deviations in texture uniformity. Similarly, B1 TR shows a marginally lower peak intensity and a more gradual decay on the right-hand side, further suggesting that the surface is not entirely homogeneous at the microscale. In contrast, B1 TL exhibits a narrower and more symmetric peak with minimal background fluctuations, indicating a relatively smoother and more uniform micro-texture. This reinforces its role as a local reference for evaluating spatial variation across the sample.

Overall, the asymmetry and side bumps observed in the B1 M and B1 TR regions imply spatial non-uniformity in surface roughness amplitude, likely due to variations in the porous texture generated during chemical etching. The optical response remains characteristic of a disordered but weakly scattering surface, as expected for a chemically textured sample modified under low-power laser conditions.

4.1.2.2 B2 Sample (2 W, 60 min)

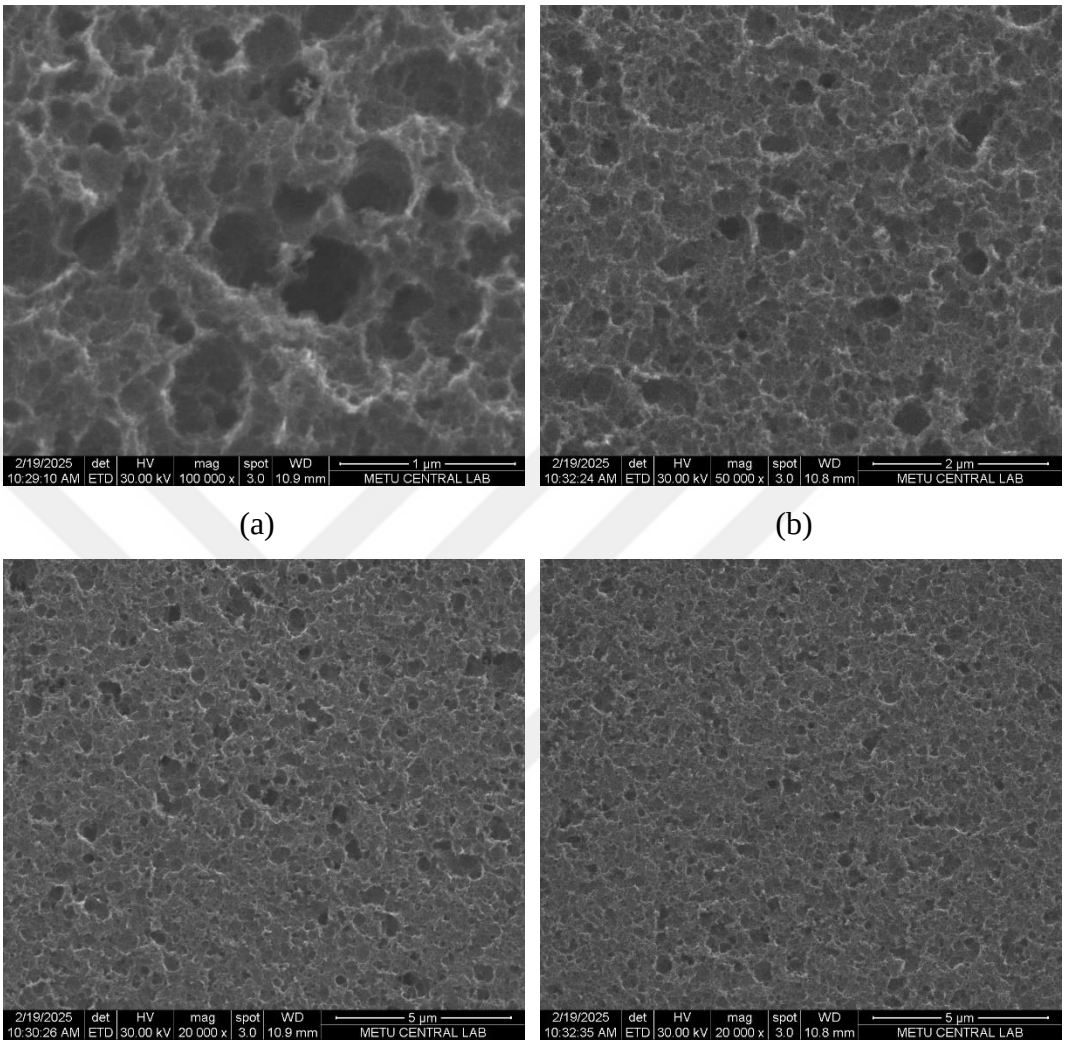

Figure 4.12 Surface morphology of the B2 sample, which was fabricated using chemical etching followed by laser irradiation at 2.0 W for 60 minutes. SEM images were taken at different magnifications to examine the surface roughness: (a) 100000× (scale bar: 1 µm), (b) 50000× (scale bar: 2 µm), (c) 20000× (scale bar: 5 µm), (d) 20000× (scale bar: 5 µm).

The SEM images of the B2 sample, processed under 2.0 W laser power for 60 minutes, reveal a significantly more developed and heterogeneous surface texture compared to B1 (Figure 4.12).

At higher magnification (Figure 4.12a–b), the surface exhibits a dense population of irregular pores and pits with varying depths and diameters. The more pronounced vertical topography suggests increased ablation or melting, likely due to the higher energy density during laser irradiation.

At lower magnifications (Figure 4.12c–d), the rough texture persists across broader areas, with visible contrast variations between regions, indicating spatial variation in laser–material interaction. These observations support the interpretation that higher laser power enhanced surface roughness by deepening and deforming the chemically etched features rather than smoothing them. The resulting morphology reflects a synergistic effect of chemical porosity and laser-induced microstructural modification, yielding a chaotic and non-periodic surface.

The evolution from B1 to B2 highlights how increasing laser power alters the balance between surface smoothing and feature enhancement, with B2 exhibiting deeper, more irregular structures that result in stronger diffuse scattering, as confirmed by ARS measurements.

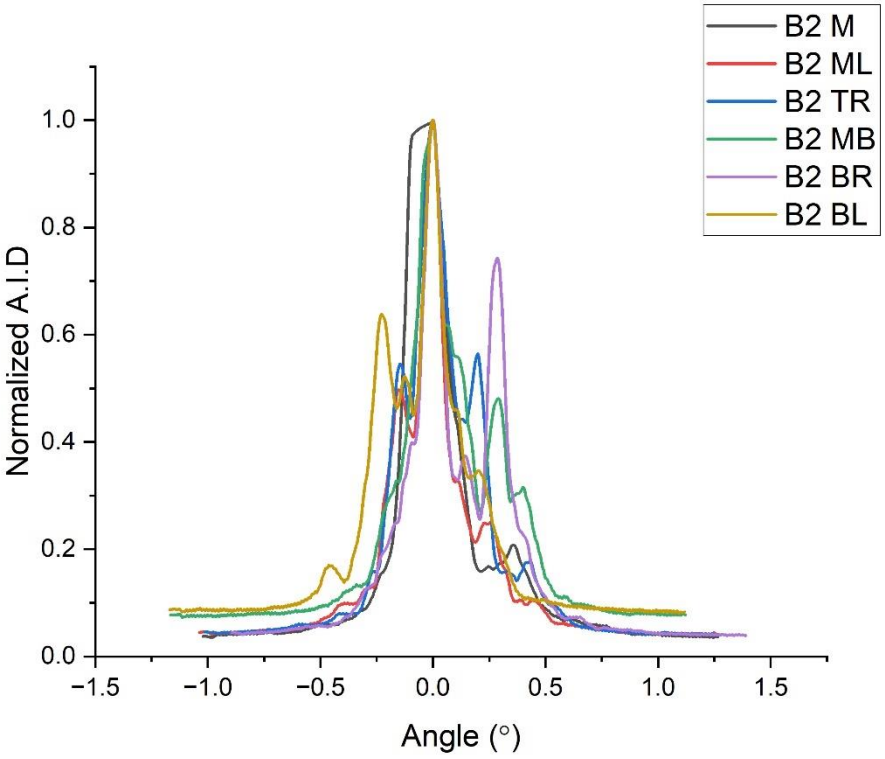

Figure 4.13 Normalized angle-resolved scattering intensity profiles measured at six different positions on the B2 sample surface: Middle (M), Middle-Left (ML), Top-Right (TR), Middle-Bottom (MB), Bottom-Right (BR), and Bottom-Left (BL).

The angle-resolved scattering profiles of B2 (Figure 4.13) exhibit strong variability across different regions of the surface, confirming the spatial inhomogeneity suggested by SEM. All profiles were normalized and laterally shifted so that their specular peaks align at 0°, enabling direct comparison. While the general shape of the scattering curves is preserved, substantial differences are observed in peak width, asymmetry, and background levels.

Notably, the B2 BL and B2 BR regions display broader profiles with multiple off-specular bumps, especially on the left side (e.g., –0.8° to –0.4°), indicating enhanced diffuse scattering due to rougher local features. In contrast, B2 M maintains a sharper

and more symmetric peak, suggesting relatively smoother morphology in that location. Regions such as B2 TR and B2 MB show intermediate behavior with gradual decay and elevated side intensities.

Overall, the ARS measurements of B2 indicate that increased laser energy resulted not only in greater surface roughness but also in larger spatial variation across the sample. This is consistent with the SEM-based interpretation and confirms that moderate laser powers can significantly affect both the depth and distribution of surface features, leading to stronger and more angle-spread diffuse scattering.

4.1.2.3 B3 Sample (2.5 W, 60 min)

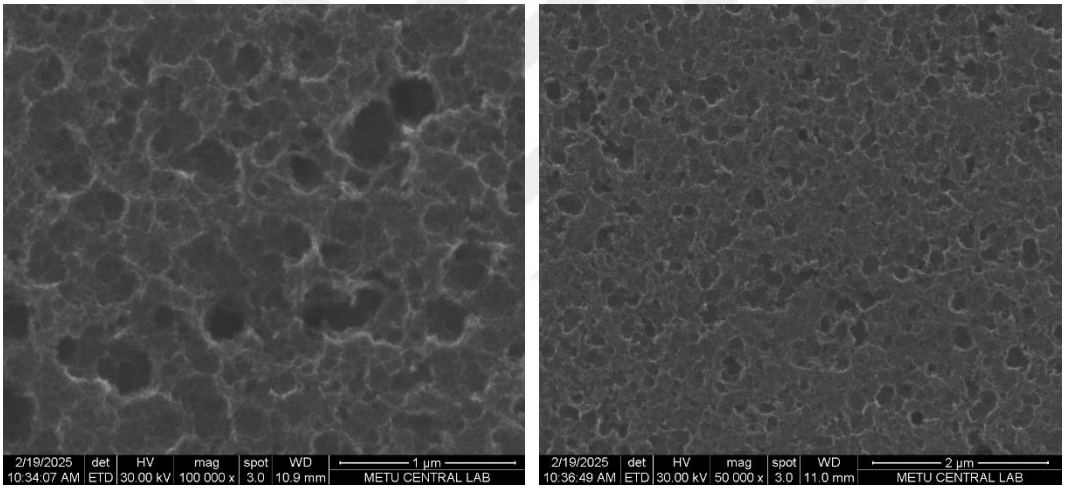

(a) (b)

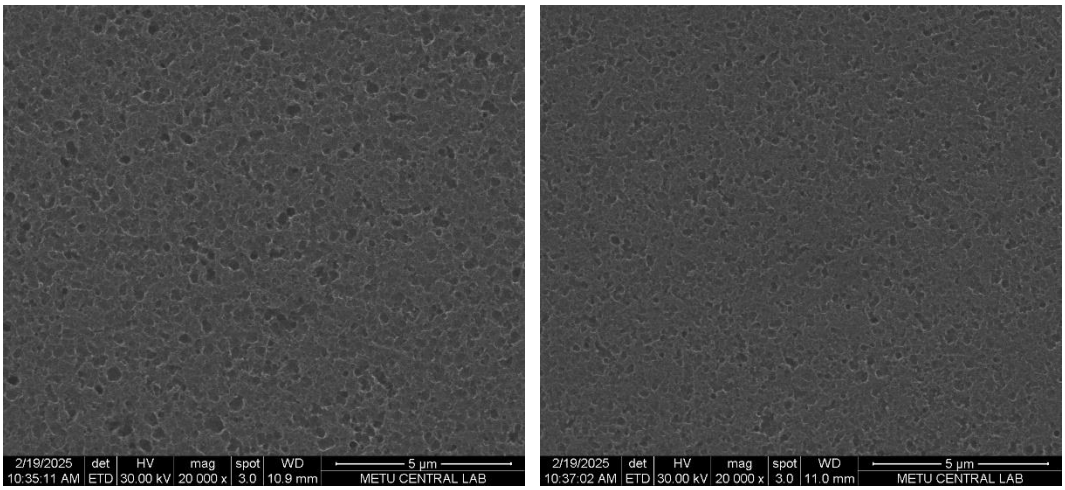

(c) (d)

Figure 4.14 Surface morphology of the B3 sample, which was fabricated using chemical etching followed by laser irradiation at 2.5 W for 60 minutes. SEM images were acquired at various magnifications to examine the surface texture: (a) 100000× (scale bar: 1 µm), (b) 50000× (scale bar: 2 µm), (c) 20000× (scale bar: 5 µm), (d) 20000× (scale bar: 5 µm).

The SEM images of the B3 sample, processed with the highest laser power in this series (2.5 W), reveal a complex and heavily textured surface morphology (Figure 4.14).

At higher magnification (Figure 4.14a–b), the surface is dominated by large, irregularly shaped pits and highly non-uniform features. These structures appear deeper and more pronounced than those in B1 and B2, indicating enhanced material ablation and more aggressive surface restructuring.

At lower magnifications (Figure 4.14c–d), the texture remains chaotic at the microscale but appears spatially consistent across broader areas. This suggests that although the laser–material interaction was more intense, it did not create macroscopic heterogeneity but instead amplified roughness in a spatially uniform manner.

Compared to B1 and B2, the B3 sample exhibits the highest level of surface roughness, with greater vertical depth and lateral irregularity. The morphology suggests that surface modification has reached a saturation point, where chemical and laser-induced effects combine to create a surface highly effective in disrupting specular reflection, a behavior confirmed by the corresponding ARS measurements.

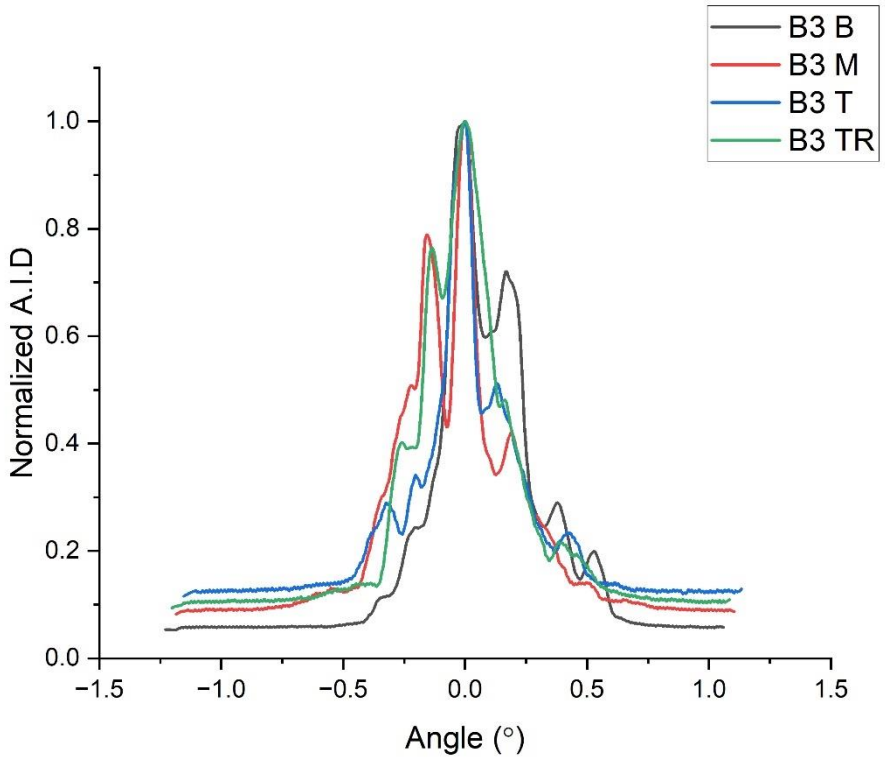

Figure 4.15 Normalized angle-resolved scattering intensity profiles measured at six different positions on the B3 sample surface: Bottom (B), Middle (M), Top (T) and Top-Right (TR)

The angle-resolved scattering profiles of B3 (Figure 4.15) show broadened peaks and stronger off-specular scattering compared to the previous samples, in agreement with the SEM observations. All profiles were normalized and laterally shifted to align their specular peaks at 0°, allowing direct comparison.

Among the measured positions, B3 B displays the broadest and most diffuse profile, with intensity extending beyond ±0.5°, indicating scattering from large or disordered surface structures. The B3 M region also exhibits elevated side lobes, especially toward negative angles, suggesting deeper or more irregular features in that area.

In contrast, the B3 T and B3 TR regions show sharper and more symmetric peaks with reduced side scattering, pointing to relatively more uniform local morphology.

Despite these regional differences, the overall shape of the scattering curves remains statistically consistent across the surface, with minor secondary features appearing at similar angular positions. This suggests that the surface roughness is random but spatially uniform in distribution. In particular, the recurrence of side lobes around –0.8° and +0.3° across multiple measurement positions implies the presence of surface structures with characteristic spatial frequencies. While the roughness appears random in position, the angular coherence of these features suggests spectral consistency, contributing to a more structured off-specular scattering behavior in the B3 sample.

The increased peak broadening and diffuse side scattering in B3 confirm that the sample is the most optically diffuse among Group B, supporting the conclusion that higher laser power enhances both the depth and spatial variation of surface roughness.

4.1.2.4 Statistical Comparison of Group B

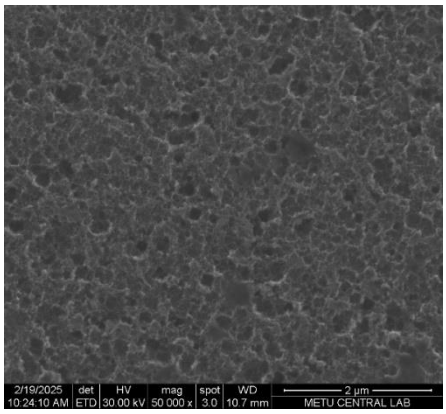

(a)

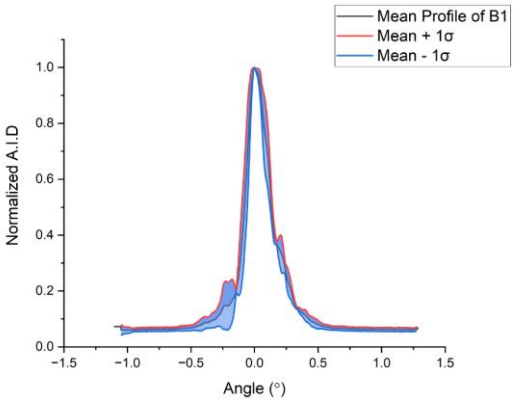

(d)

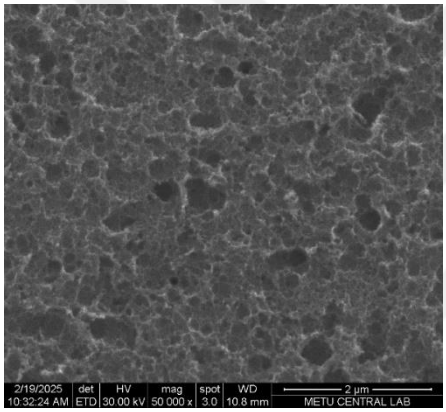

(b)

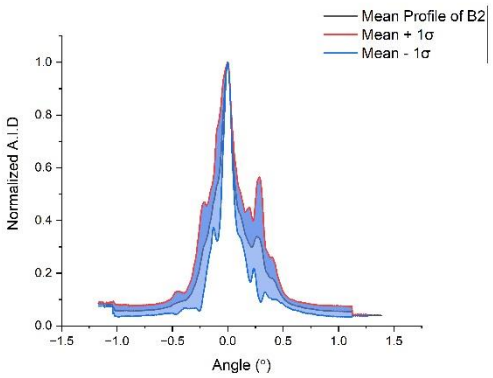

(e)

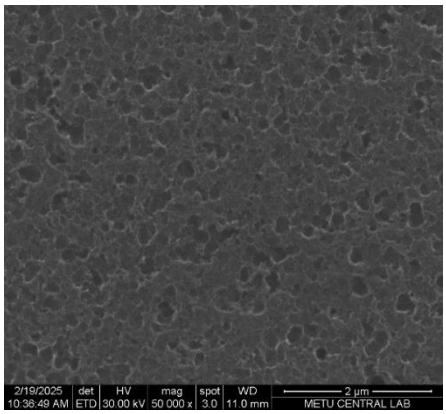

(c)

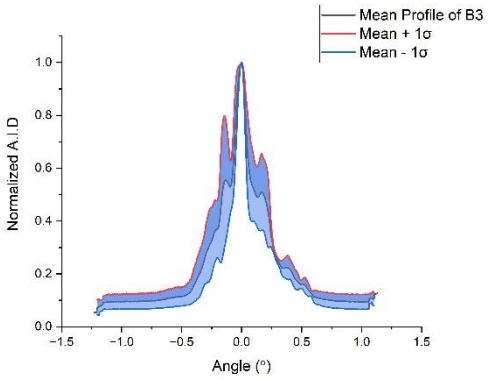

(f)

Figure 4.16 Statistical comparison of Group B samples using standard deviation profiles and representative SEM images. Left: SEM morphology at 50000× (scale bar: 2 μm). Right: Mean angle-resolved scattering profiles with ±1σ standard deviation.

To evaluate the surface uniformity and angular scattering variability within each sample, the mean angle-resolved scattering intensity profiles along with ±1 standard deviation (σ) envelopes were plotted for B1, B2, and B3 in Figure 4.16. These representations provide insight into both the average optical response and the spatial consistency of the scattering behavior across the measured positions.

The B1 sample, which was processed using 1.5 W laser power for 60 minutes, exhibits the narrowest mean peak and the tightest standard deviation band around the specular angle, indicating highly consistent scattering behavior across the surface. The minimal spread between the mean ±σ boundaries implies that the surface morphology is laterally uniform, with only minor fluctuations in feature geometry or roughness. This observation is consistent with the SEM images showing a uniformly rough, chemically textured surface with minimal laser-induced modification.

In contrast, the B2 sample, which received 2.0 W laser exposure for 60 minutes, shows a broader mean peak and noticeably higher standard deviation values, particularly on the left shoulder of the specular peak. This broader spread reflects greater spatial variability in the surface features, likely due to the use of higher laser power during processing. The elevated σ in off-specular regions suggests that some areas exhibit enhanced light scattering due to deeper or more irregular surface structures, as supported by the SEM images.

The B3 sample, which was irradiated at the highest laser power level of 2.5 W for 60 minutes, displays the most diffuse mean scattering profile among all three samples, yet maintains a relatively well-aligned ±σ band across the angular range. This indicates that despite having the roughest and most complex microstructure, the

scattering behavior remains statistically consistent across the sample. The broader but coherent standard deviation envelope suggests that the roughness level is saturated throughout the surface and varies less abruptly between regions. This aligns with earlier observations that B3 exhibits a uniformly chaotic structure, where local irregularities are randomly distributed but result in a coherent angular response across the surface.

In summary, while B1 demonstrates low spatial variation and high uniformity, B2 shows significant heterogeneity due to localized structural differences. B3, on the other hand, combines high diffuse scattering with stable angular behavior, suggesting that increased laser power leads to a saturated roughness regime, where local features vary randomly but the overall scattering response remains consistent.

4.2 Diffraction Orders and Periodicity

The spatial periodicity of surface structures can be characterized through two complementary approaches: morphological analysis in the frequency domain and optical scattering in the angular domain [21]. In this section, 2D fast Fourier transforms (FFT) were applied to SEM images to estimate dominant spatial frequencies and generate a reference for surface periodicity. This frequency-domain analysis provides a geometry-based benchmark, which is then compared against the angularly resolved scattering data to evaluate whether the observed diffraction features are consistent with the physical structure. Peaks in the FFT spectrum correspond to periodic components of the structure, where higher spatial frequencies indicate finer surface features. These results offer a geometry-based benchmark that will later be compared with angularly resolved scattering data.

Based on this reference, ARS measurements were analyzed to determine whether the experimentally observed angular peaks align with the predicted periodicities. The angular distribution of scattered light from periodic surfaces carries valuable

information about the underlying structural regularity. In particular, the appearance of discrete diffraction orders serves as a direct optical signature of surface periodicity. This section outlines the experimental approach used to extract surface period from ARS data and verify the presence of periodic features through diffraction behavior.

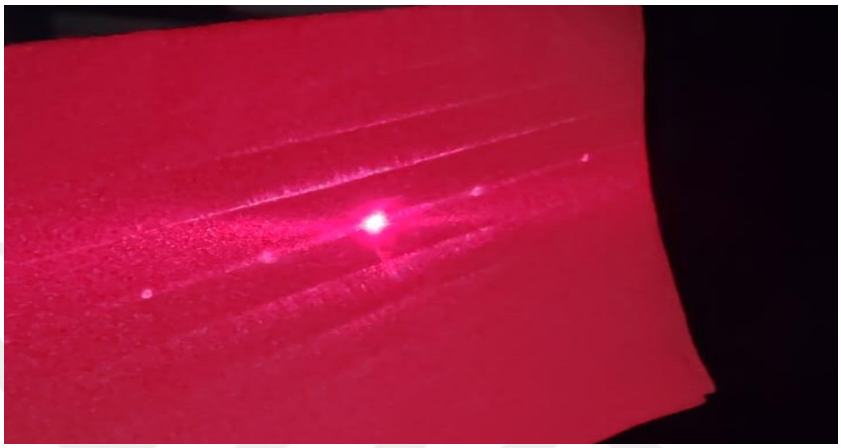

Figure 4.17 Optical diffraction pattern observed during ARS measurements, showing multiple well-defined diffraction orders. The visibility and angular separation of the spots qualitatively indicate the presence of periodic surface features.

Samples A1 to A6 were designed to explore the effect of fabrication parameters, specifically laser scanning speed and hatch distance, on surface periodicity. While A1, A2, and A3 share the same hatch distance of 4 μm and differ in scanning speeds, 5, 7, and 10 m/s respectively; A4, A5, and A6 were fabricated with different hatch distances of 7 μm, 1 μm, and 1 μm, and scanning speeds of 10 m/s, 5 m/s and 10 m/s. This variation allows for a broader assessment of how surface geometry influences diffraction behavior, particularly the emergence and angular distribution of diffraction orders.

All angular scans were performed between 45° (specular direction) and 23.75°, covering the expected range for first and second order diffraction peaks based on the

surface period. This angular window was selected to minimize the effects of detector saturation near the specular reflection, thereby ensuring more reliable peak detection in the surrounding angular range.

Since the primary goal in this section is to determine angular peak positions, normalized A.I.D values were used. This normalization preserves angular information and ensures consistency in peak position analysis, regardless of overall intensity levels.

To quantitatively estimate the surface period, the angular positions of the first-order diffraction peaks were inserted into the grating equation (4.1):

$$d = \frac{m\lambda}{(sin\theta_i + sin\theta_m)} \tag{4.1}$$

where d is the surface period, λ = 650 nm is the laser wavelength, θ_i = 45° is the fixed incident angle, and θ_m denotes scattered light of m-th order measured with respect to the surface normal.

The ARS measurements used for this analysis were obtained from five different locations (middle, top, bottom, left, and right) on samples A1, A2, and A3, as standardized in Section 4.1 and illustrated in Figure 4.1. This allowed a direct comparison between the angular positions of diffraction orders at different regions, which can also be cross-checked with the uniformity results presented earlier.

Samples A4, A5 and A6 were not analyzed for surface uniformity; instead, they were included to assess the general impact of laser speed and hatch distance on surface periodicity. This distinction is important, as the aim was not to evaluate spatial uniformity but to examine how fabrication parameters influence the regularity of the surface structure. To prevent local surface defects from biasing the interpretation, multiple regions were checked during measurements, and no significant deviations were observed. Therefore, using only the central-region data was considered sufficient for the intended analysis.

4.2.1 A1, A2 and A3 Samples (Laser Speeds 5 m/s, 7 m/s, 10 m/s; Hatch Distances 4 µm)

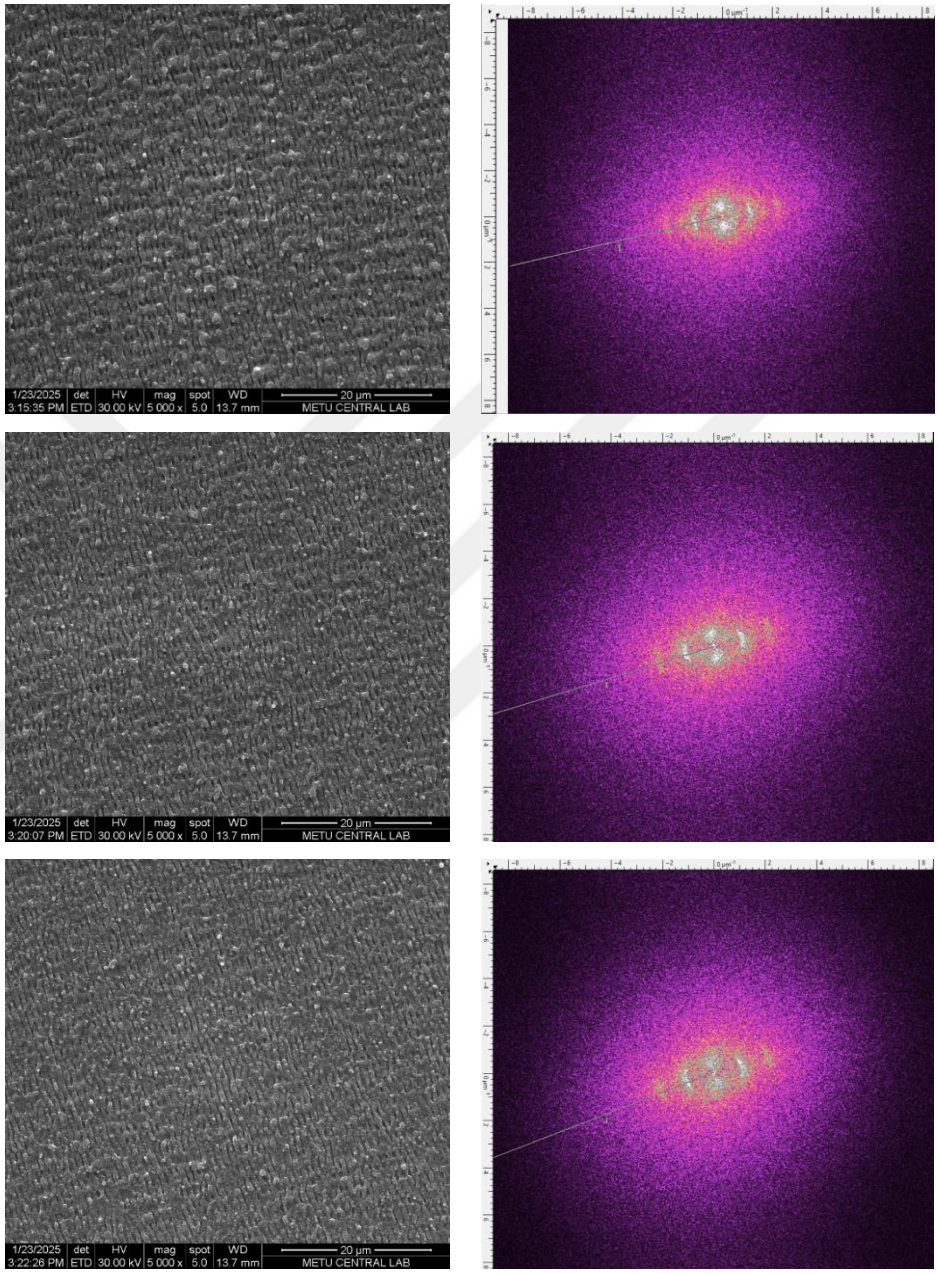

Figure 4.18 SEM-FFT analysis of A1, A2 and A3 Samples. Left: SEM images at 5 000× (scale bar: 20 µm) Right: 2D FFT modules (Hann window, mean subtracted) with radial profile.

A1

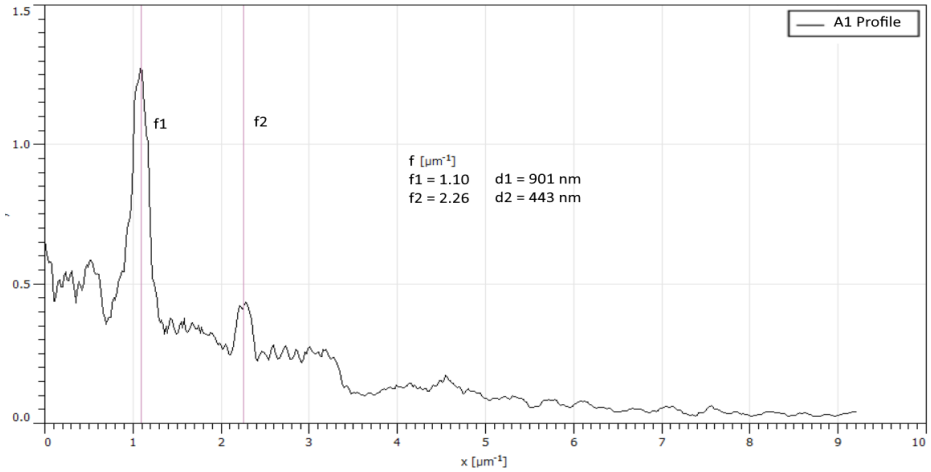

A2

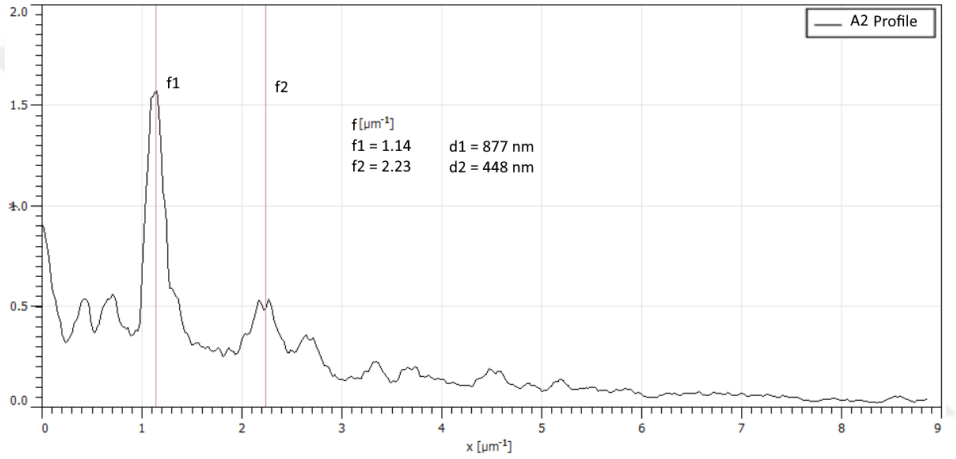

A3

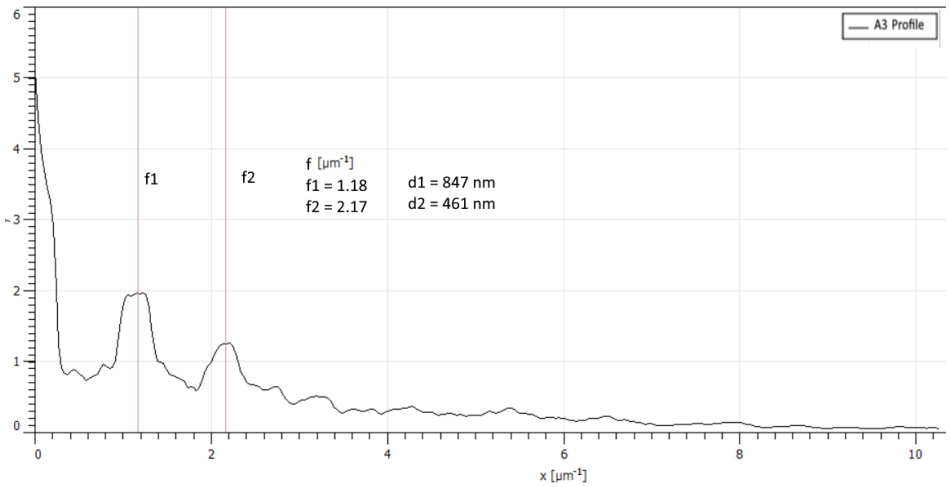

Figure 4.19 Line profiles of FFT modulus as a function of spatial frequency $f\ (um^{-1})$ with annotated peaks of samples A1, A2 and A3.

To investigate the surface periodicity of the A1, A2, and A3 samples, 2D FFT were applied to their 20 μm scale SEM micrographs (Figure 4.18). In all cases, the FFT modulus spectrum was computed using a Hann window with mean subtraction, and a radial line profile was extracted to visualize dominant spatial frequencies (Figure 4.19). Three main peaks were consistently observed in the line profiles for each sample as shown in Table 4.1.

Table 4.1 Dominant Spatial Frequencies and Calculated Periods for A1–A3

	A1	A2	A3
$f_1(um^{-1}) \rightarrow d_2(nm)$	$1.10 \rightarrow \approx 901$	$1.14 \rightarrow \approx 877$	$1.18 \rightarrow \approx 847$
$f_2(um^{-1}) \rightarrow d_3(nm)$	$2.26 \rightarrow \approx 443$	$2.23 \rightarrow \approx 448$	$2.17 \rightarrow \approx 461$

The frequency f_1 corresponds to the primary LIPSS wavelength, and f_2 represents its second harmonic. These are the most prominent and sharp features in the FFT spectra, indicating a well-defined submicron periodic structure across all samples.

Although additional peaks appear in some profiles, particularly in the lower frequency region, these features were not consistent across different line orientations or positions. Their shape and position varied significantly with minor adjustments in the FFT line extraction, suggesting they are not structurally robust. A similar behavior is observed for the expected hatch-related frequency at $f = 0.25\, um^{-1}$, which corresponds to a 4 μm period. This component appears within the low-frequency region but fails to emerge as a distinct or reproducible peak. Its proximity to the DC component leads to blending with the central specular intensity, making it particularly sensitive to profile location.

Altogether, this variability limits the reliability of 1D FFT line profiles in identifying long-period surface modulations. While such features may still exist in the structure, their confirmation requires alternative optical methods such as angle-resolved scattering, which are discussed in the following section.

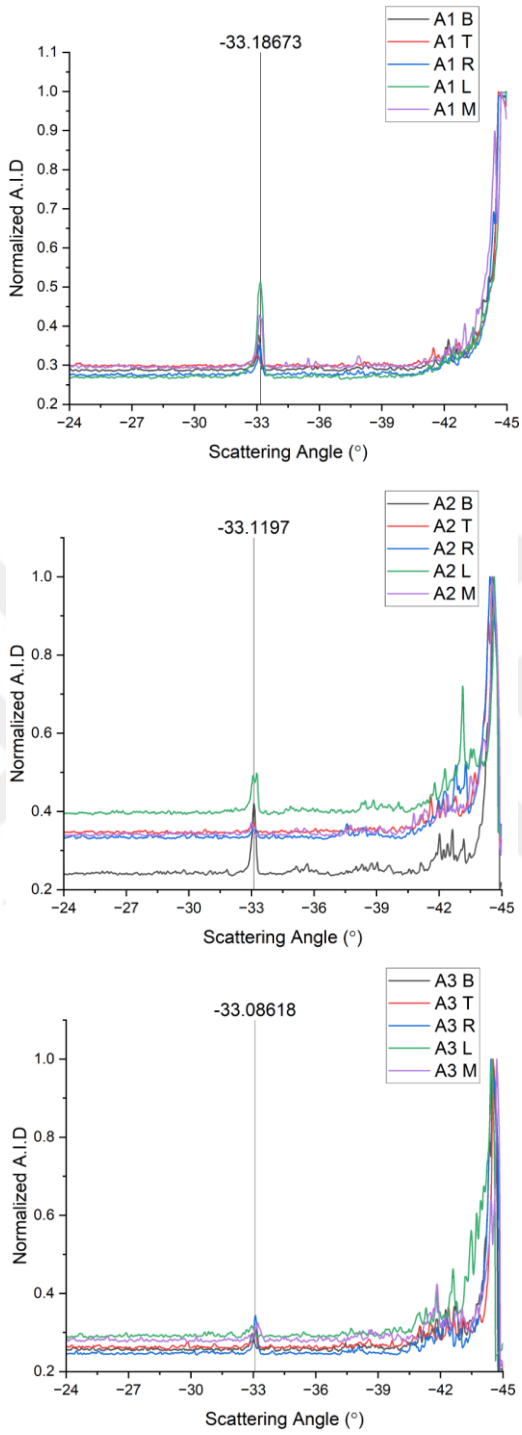

Figure 4.20 ARS profiles of A1, A2, and A3 around specular and side diffraction peaks, measured from five different surface positions. Vertical lines indicate the angular positions of observed diffraction peaks.

Table 4.2 Grating Periods Determined from Wide Angle Measurement

Samples	Peak Angle θ_s (°)	Order, m	d (nm)
A1	-33.18673	1	4075.2
A2	-33.1197	1	4047.6
A3	-33.08618	1	4031.1

Figure 4.20 shows the ARS profiles of A1, A2, and A3 samples, collected from five distinct surface positions. In all three samples, a well-defined diffraction peak consistently appears near $\theta_s \approx -33.1°$, corresponding to a first-order diffraction feature. The calculated periods, based on the grating equation, are summarized in Table 4.2, yielding values close to 4 μm across all samples.

These results confirm the presence of a periodic surface modulation at ~4 μm scale, which is not clearly captured in the FFT spectra due to limitations discussed earlier. Specifically, the expected spatial frequency component at $f = 0.25\ um^{-1}$ was blended with the DC region in the frequency domain and could not be consistently resolved through 1D FFT profiles. Nevertheless, the ARS measurements provide direct angular evidence of this long-period structure, demonstrating the complementary value of diffraction-based analysis.

Moreover, the high degree of overlap among the five positional scans in each sample suggests good spatial spatial uniformity of the 4 μm periodic pattern. This observation is consistent with the statistical analysis discussed in 4.1.1.4, where A1–A3 samples showed relatively uniform angular scattering behavior.

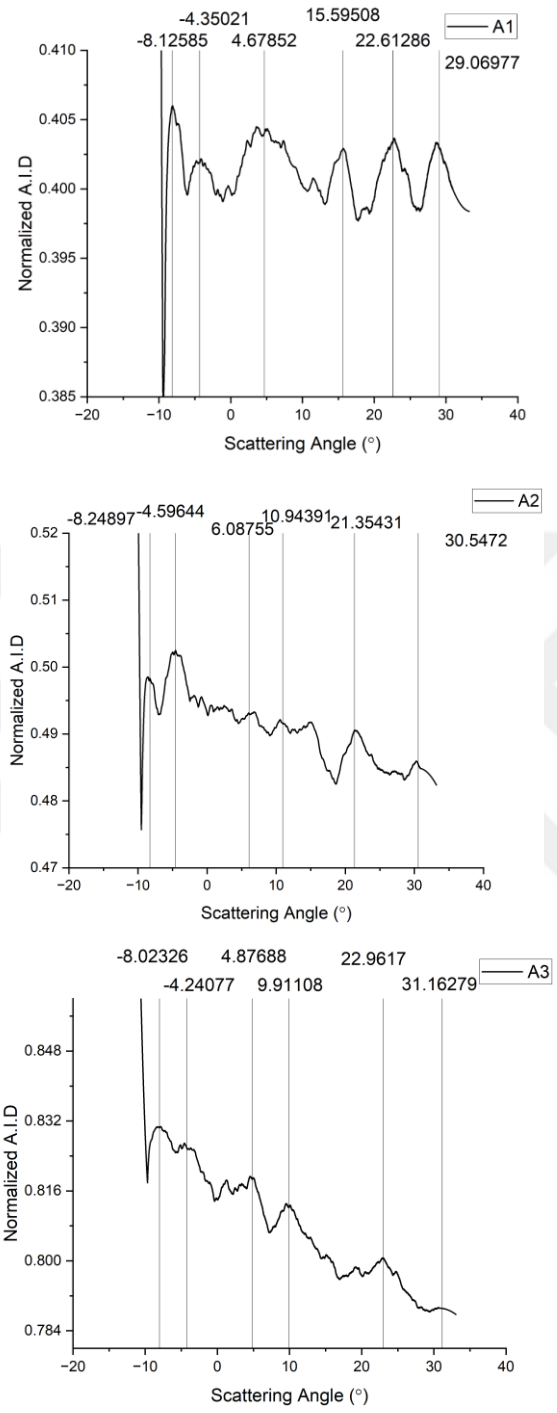

Figure 4.21 Wide-angle ARS measurements of A1, A2, and A3 showing multiple diffraction peaks at higher scattering angles. Vertical lines indicate the angular positions of observed diffraction peaks.

Table 4.3 Period Estimation for A1, A2 and A3 Samples Based on Diffraction Orders

Angle (°)			Order	Period (nm)		
A1	A2	A3		A1	A2	A3
-8.12585	-8.24897	-8.02326	**1**	**1148.9**	**1153.3**	**1145.3**
			2	**2297.8**	**2306.5**	**2290.6**
			3	3446.7	3459.8	3435.9
-4.35021	-4.59644	-4.24077	**1**	**1029.7**	**1036.9**	**1026.6**
			2	**2059.4**	**2073.9**	**2053.2**
			3	3089.1	3110.8	3079.8
4.67852	6.08755	4.87688	**1**	**824**	**799.3**	**822.1**
			2	**1648.3**	**1598.5**	**1644.2**
			3	**2472.5**	**2397.8**	**2466.3**
15.59508	10.94391	9.91108	1	666	724.7	737.4
			2	1332	1449.4	1474.7
			3	**1998**	**2174.1**	**2212.1**
22.61286	21.35431	22.9617	1	595.5	606.7	591.5
			2	**1190.9**	**1213.3**	**1183.0**
			3	1786.4	1820.0	1774.5
			4			
29.06977	30.5472	31.16279	**1**	**544.9**	**534.8**	**529.9**
			2	**1089.7**	**1069.7**	**1059.8**
			3	**1634.6**	**1604.5**	**1589.7**

In Figure 4.20, the specular-centered measurements show that at higher scattering angles, it becomes increasingly difficult to resolve peaks corresponding to lower spatial periods. To address this, the measurements in Figure 4.21 were taken starting from the estimated first-order diffraction angle. After filtering and normalization,

several peaks became distinguishable. These graphs aim to identify angular positions of diffraction peaks, and no quantitative interpretation of intensity is attempted, as it is affected by various factors and does not directly reflect diffraction efficiency. In Table 4.3, the angular positions of the observed peaks in A1, A2, and A3 samples are listed along with the corresponding surface periods calculated for the first three diffraction orders. By comparing these values across samples and orders, one can identify which periods consistently appear and how different orders of the same structure may overlap to form stronger peaks. The color-coded values in the table further help to track repeating periods and evaluate the potential contribution of multiple structures to the observed scattering behavior.

Each peak in the angular scattering profiles may correspond to different diffraction orders of different surface periods. Since the measurements shown in this graph were taken by scanning 45° forward from the estimated m = 1 angle of a 4000 nm structure, it is important to consider that higher-order peaks of smaller periods may also appear in this region. Multiple orders from different structures can overlap and form stronger combined peaks. For this reason, ARS measurements offer a wide and layered insight into the surface morphology. Sharp and strong peaks may indicate the presence of higher diffraction orders, and the broader width of a peak may suggest overlapping contributions from multiple orders. If a peak is significant, it is expected that its lower-order counterparts also appear in the scan, which can help identify the actual period more confidently.

The peak around −8.1°, for instance, aligns closely with the expected m = 1 position of a 4000 nm period. While this proximity may reduce certainty, the fact that the peak is strong and follows a noticeable drop between neighboring points supports the existence of a true structure. The same region also shows a corresponding peak in both A2 and A3 samples. As discussed earlier, the surface morphologies of A1, A2, and A3 are relatively similar, and the consistent appearance of this peak across samples strengthens the interpretation. Peaks corresponding to ~1200 nm periods

and their higher orders also align with this region, pointing toward the presence of such a structure.

Around −4.3°, the measured periods are close to 1000 nm, and several higher-order values from different structures seem to converge there. This could imply a base period of ~1000 nm, but it could also result from the superposition of orders from smaller (~500 nm) periods. The relatively steep rise in this peak in A1 compared to the weaker counterparts in A2 and A3 supports the interpretation that this is a combined peak of multiple orders. The 4–6° range shows moderate peaks, but their lower intensity suggests that 400–500 nm may not be the dominant base period across the surface. At 10° and 15°, variations in peak intensity between samples indicate a lack of strong periodicity in the ~700 nm range. On the other hand, strong peaks around 22° may represent higher orders of the structures visible near −8°. Peaks near 30° also appear more prominent than their surroundings and may correspond to high-order contributions from periods around −4° or +4°.

All calculated period values and their potential harmonic alignments are highlighted in the table using color coding. Most of the prominent peaks occur at angular positions that correspond to integer multiples of a value between 400–500 nm. In particular, the peaks around −8°, −4°, 4°, 22°, and 30° strongly suggest the presence of a ~450 nm base period on the surface. This interpretation is also supported by the SEM-FFT results, which revealed strong frequency components around 450 and 870 nm. Together, these results validate the use of ARS as a reliable technique to resolve surface periodicities that may not be easily extracted from SEM-based frequency-domain analysis.

4.2.1 A4, A5 and A6 Samples (Laser Speeds 10 m/s, 5 m/s, 10 m/s; Hatch Distances 7 µm, 1 µm, 1 µm)

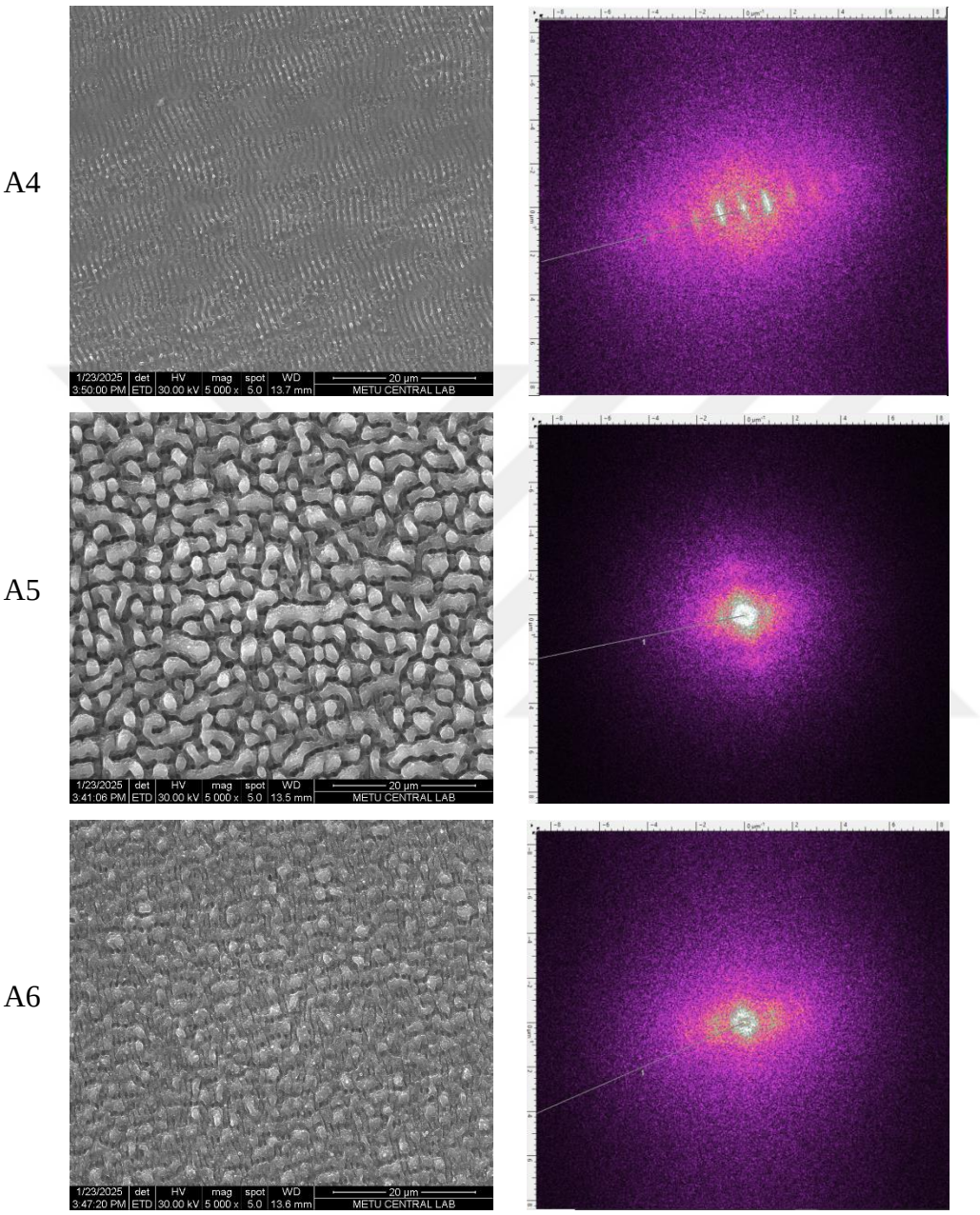

Figure 4.22 SEM-FFT analysis of A4, A5 and A6 Samples. Left: SEM images at 5 000× (scale bar: 20 µm) Right: 2D FFT modules (Hann window, mean subtracted) with radial profile.

A4

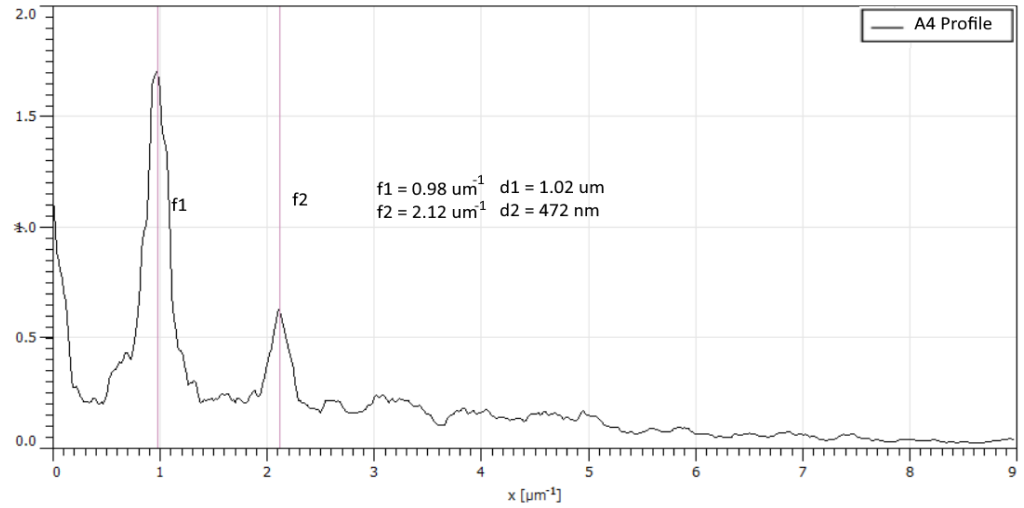

A5

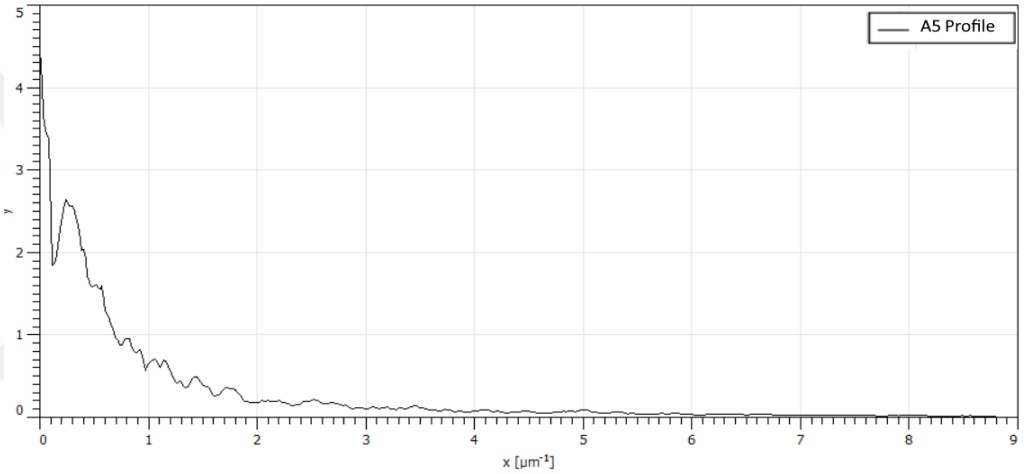

A6

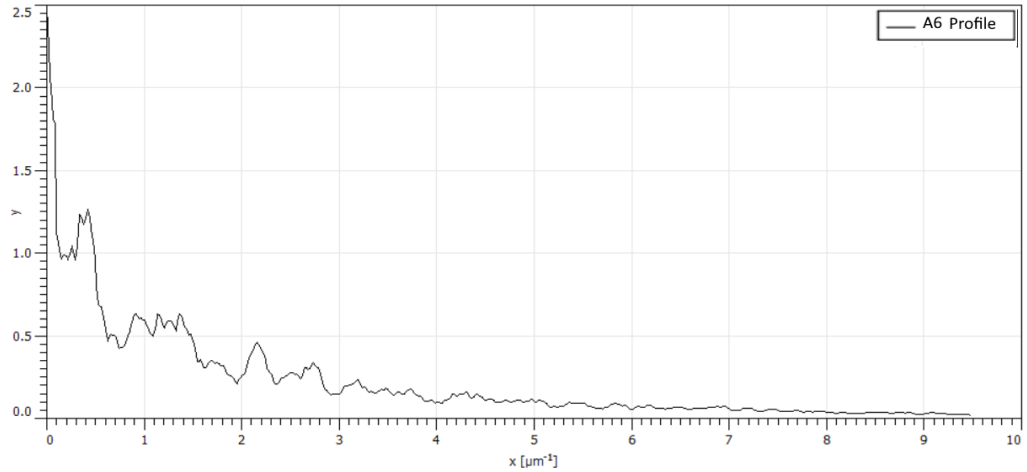

Figure 4.23 Line profiles of FFT modulus as a function of spatial frequency $f\ (um^{-1})$ with annotated peaks of samples A4, A5 and A6.

Samples A4, A5, and A6 were processed with different laser speeds and hatch distances, which resulted in clearly different surface morphologies and optical responses. The SEM image in Figure 4.22 of A4 shows regular, straight traces with uniform spacing and a clear directional pattern, indicating a well-formed grating-like structure. In contrast, A5 and A6 have irregular, worm-like surface textures without any visible periodicity. In Figure 4.23, the 2D-FFT profile of A4 shows two distinct peaks at $f_1 = 0.98\,um^{-1}$ and $f_2 = 2.12\,um^{-1}$, confirming the presence of a periodic structure $d_1 = 1.02\,um$ and $d_2 = 472\,nm$. A5 and A6, however, do not exhibit any sharp frequency components, A5 shows a monotonically decreasing spectrum, and A6 has only a weak and broad feature around $f = 0.6\,um^{-1}$, suggesting very low coherence. However, this slight peak may be misleading since it appears close to the specular region and might not represent a real periodic component of the surface.

Although A1 and A3 were processed using the same laser speeds as A5 and A6 (5 m/s and 10 m/s, respectively), their surface structures exhibit significantly more regular and well-aligned patterns. This contrast is primarily attributed to the difference in hatch spacing: A1 and A3 were fabricated with a spacing of 4 μm, whereas A5 and A6 used a much smaller value of 1 μm. Such tight spacing increases the overlap between adjacent scan lines, which can lead to local overheating, excess energy accumulation, and material overprocessing. As a result, the surface morphology becomes highly irregular, especially at lower speeds (A5), and even at higher speeds (A6), the overlap still hinders the formation of coherent periodic features. These observations suggest that the loss of periodicity in A5 and A6 is more strongly influenced by hatch spacing than by scanning speed alone.

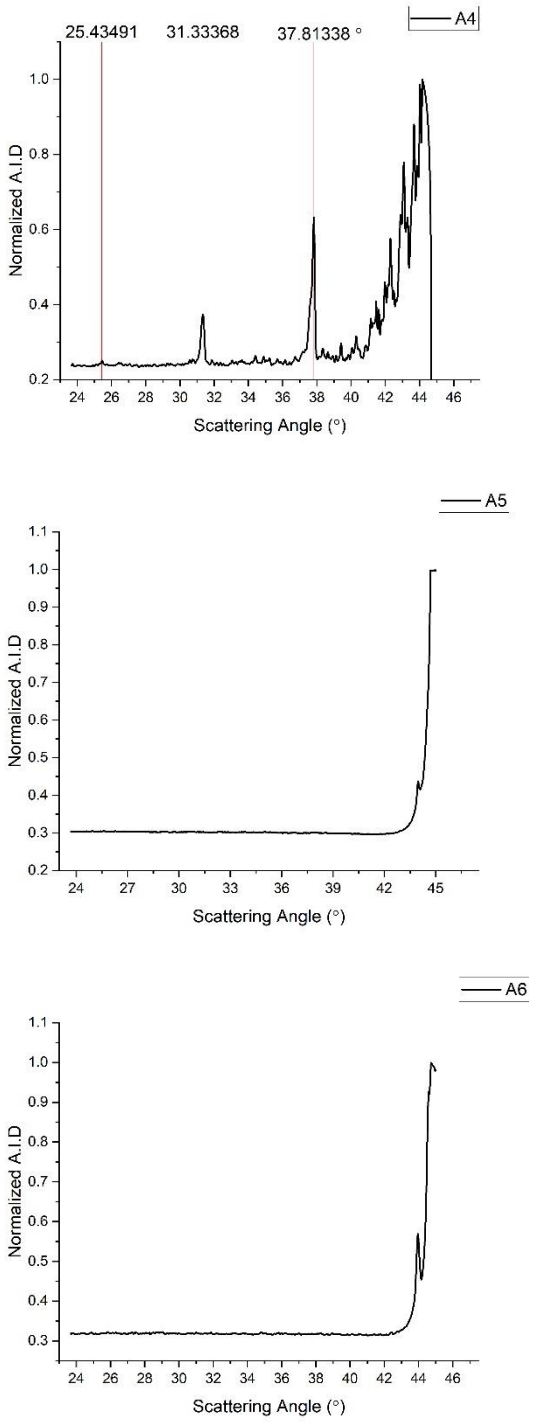

Figure 4.24 ARS profiles of A4, A5, and A6 samples measured around the specular region.

Sample A4 displays multiple distinct peaks at lower angles (e.g., 25.4°, 31.3°, and 37.8°), which suggest the presence of diffraction from surface features with relatively large spatial periods on the order of several micrometers.

Table 4.4 Dominant Spatial Frequencies and Calculated Periods for A1–A3

Samples	Peak Angle θ_s (°)	Order, m	d (nm)
A4	25.4	3	7026
	31.3	2	6925
	37.8	1	6915

In contrast, A5 and A6 exhibit only a strong specular peak with no observable side orders, indicating a lack of long-range periodicity or coherent surface patterning at the scale resolved by angle-resolved scattering. This supports the interpretation of a more disordered surface morphology for these samples.

4.3 Surface Roughness and Angle-Resolved Scattering Behavior

In contrast to the localized angular scans presented in Section 4.1.2, which focused on narrow specular regions to assess surface uniformity, this section examines the broader angular scattering behavior of Group B samples over an extended range (10°–120°), including measurements centered around 45°, corresponding to the specular reflection angle.

This wider field of observation enables a more comprehensive analysis of how surface roughness amplitude and structural complexity affect the distribution of scattered light, especially in regions where diffuse and angle-spread behavior dominates. By comparing the optical responses of B1, B2, and B3, fabricated under increasing laser powers, this section highlights how progressively rougher surfaces give rise to broadened peaks, elevated background levels, and more widespread angular scattering. These features are interpreted alongside corresponding SEM and AFM images to establish the relationship between morphological evolution and wide-angle optical behavior. Altogether, these results not only highlight the sensitivity of ARS measurements to subtle morphological changes but also provide insight into the transition from partially ordered to fully irregular surface states. Therefore, such observations are critical for understanding how fabrication parameters influence optical functionality in roughened microstructured surfaces.

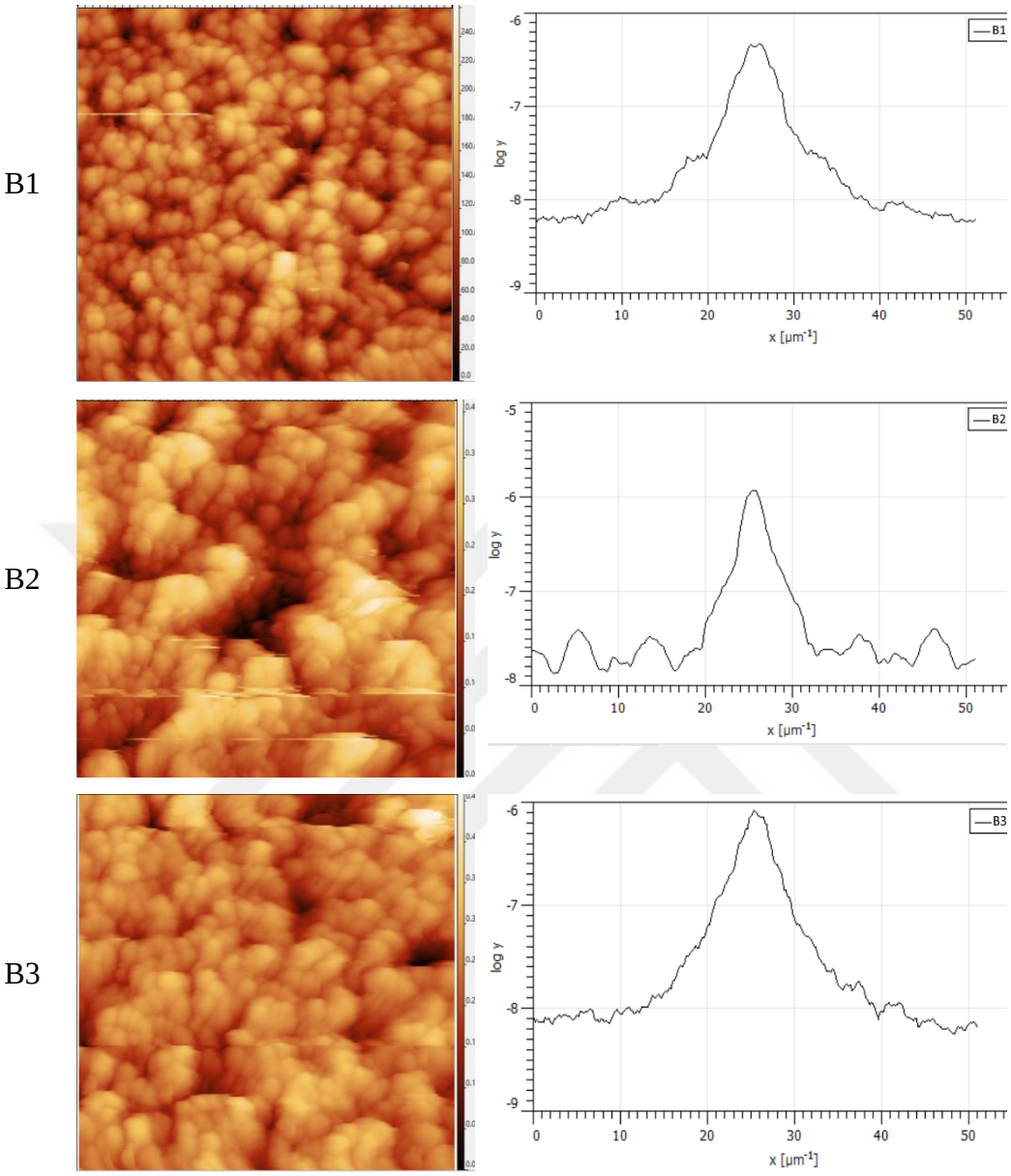

Figure 4.25 AFM topography images and log-transformed FFT profiles of Group B samples, showing surface structure and dominant spatial frequencies.

The AFM topography images and their corresponding log-transformed FFT profiles (Figure 4.25) illustrate the morphological evolution of Group B samples.

B1 presents a relatively ordered and isotropic surface, as evidenced by a smooth AFM map and a symmetric FFT peak centered around a dominant spatial frequency.

In contrast, B2 exhibits significantly increased surface roughness and irregularity. This is reflected in both the AFM-derived roughness value (Sq = 61.89 nm, the highest among the group) and the FFT profile, which shows a sharper, more pronounced peak with multiple side- lobe fluctuations, indicating a complex mixture of spatial frequencies and microstructural disorder. B3 has a slightly lower RMS roughness (Sq = 48.61 nm), but its FFT spectrum appears broader and smoother than B2's, suggesting that B3 may feature softer, more spatially extended surface modulations. This interpretation is also consistent with the narrow-angle scattering profiles in Section 4.1.2.4 where B3 displays a wider but less sharply defined specular peak compared to B2, further supporting the presence of large-scale surface variations with reduced local sharpness.

These morphological distinctions align well with the wide-angle scattering behavior observed in the ARS profiles. As roughness increases from B1 to B3, the angular distributions reveal elevated tails, increased background levels, and more pronounced side lobes, particularly in B2. These features indicate enhanced diffuse scattering driven by microstructural complexity. Importantly, this trend is also evident in the statistical ARS analysis shown in Section 4.1.2.4, where B2 exhibits the highest profile deviation and secondary angular features in the ±1.5° region. This consistency across narrow- and wide-angle measurements supports the interpretation of B2 as the roughest and most structurally complex surface among the group.

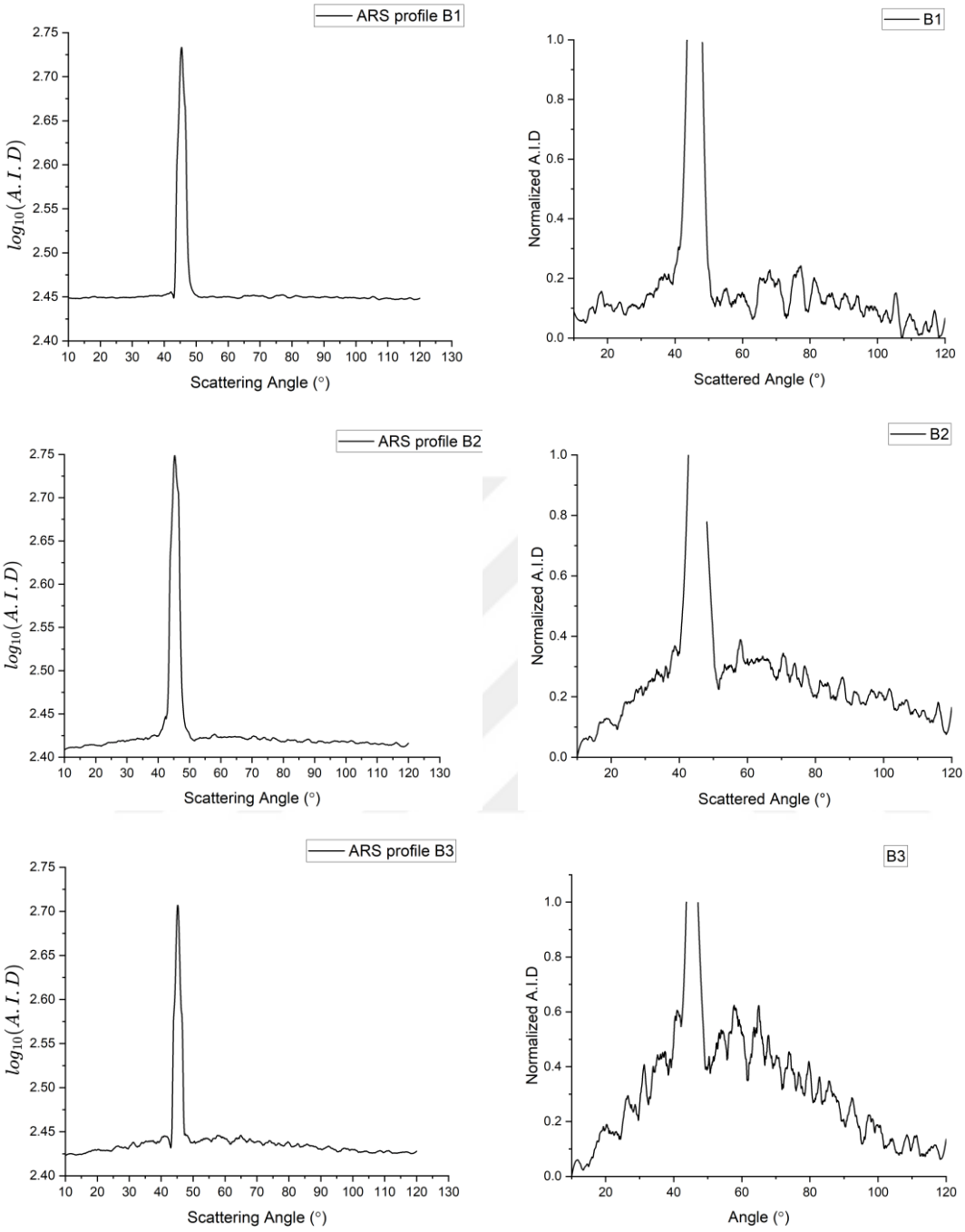

Figure 4.26 Wide-angle ARS profiles of Group B samples (B1–B3), showing both log-transformed and normalized scattering distributions.

To investigate the relationship between surface morphology and angular light scattering beyond the specular region, two complementary forms of ARS data processing were utilized. First, the raw angular intensity data were log-transformed to compress the dynamic range while preserving the relative peak intensities, allowing specular and background features to be visualized on the same scale. Second, a filtered and specular-removed version of the data was normalized to unity, emphasizing the distribution and frequency of secondary peaks across the wide-angle range (10°–120°). While absolute intensity comparisons are not valid due to these transformations, the structural differences between samples remain evident.

The angular scattering distributions presented in Figure 4.26 provide complementary insights into the effect of surface roughness on light scattering. The log-transformed ARS profiles (left column) compress the dynamic range of the signal, allowing low-intensity scattering beyond the specular region to be visualized. In this representation, B1 exhibits a steep intensity drop-off and flat background, consistent with a smooth, ordered surface. In contrast, B2 and B3 show elevated background levels and broader angular features, reflecting enhanced diffuse scattering driven by microstructural disorder. These trends correlate strongly with the AFM roughness values, where B2 exhibits the highest RMS roughness (Sq = 61.89 nm), and also with the FFT profiles in Figure 4.25, in which B2 displays the most fragmented and high-frequency-rich spectral content. While B3 has a slightly lower roughness (Sq = 48.61 nm), its FFT spectrum is broader and smoother than B2's, suggesting the presence of more spatially extended surface modulations.

The normalized ARS profiles (right column) highlight angular distribution shape by removing absolute intensity differences. Here, B1 shows a narrow, symmetric specular peak, while B2 and B3 display asymmetric profiles with multiple side lobes, indicating enhanced angular diversity in scattered light. This angular broadening and fluctuation in B2 are consistent with the statistical specular-region analysis in

Section 4.1.2.4, where B2 exhibits the highest standard deviation and most pronounced deviations from the mean profile.

Furthermore, this morphological trend is visually supported by the SEM images: both B1 and B3 exhibit more compact and homogeneous surface patterns, while B2 clearly presents a more irregular and porous texture, indicative of elevated roughness. This agreement across SEM, AFM, FFT, and ARS datasets reinforces the conclusion that B2 is the roughest and most structurally complex surface among the group. Altogether, these findings confirm that angular scattering, especially in the wide-angle regime, serves as a sensitive indicator of both the amplitude and spectral distribution of surface roughness.

CHAPTER 5

CONCLUSION

This study sets out to develop a practical, fast, and contactless optical method for evaluating microscale surface textures using angle resolved scattering. The main goal was to determine whether surface features such as periodicity, uniformity, and roughness could be identified through scattering profiles, without the need for expensive imaging tools, elaborate sample preparation, or invasive contact. A custom-built measurement system was designed and applied to laser-structured silicon surfaces, and the resulting angular scattering profiles were systematically analyzed in relation to surface morphology observed in SEM and AFM data.

The results demonstrated that scattering behavior is strongly influenced by surface structure. Periodic patterns produced clear diffraction peaks, and their angular positions corresponded well with spatial frequencies extracted from FFT analysis of SEM images. Surface uniformity was assessed through the sharpness, symmetry, and reproducibility of the specular region across different locations. For surfaces with irregular or complex textures, the angular scattering profiles exhibited broadened peaks and elevated background levels, which matched the trends observed in AFM topographies and log-transformed FFT spectra. These outcomes confirmed that angle resolved scattering can capture meaningful differences in surface morphology and serve as an effective optical indicator.

Despite the successful application of the method, there are some limitations in the current setup. The angular resolution is limited by motor step size, and signal stability at high gain settings may affect the clarity of weak features. The effects of polarization were not directly controlled, and alignment sensitivity of the photodiode

and fiber may introduce intensity fluctuations. Nonetheless, the system performed reliably across a wide range of surface types and provided consistent results, even when morphological differences were subtle.

Future improvements may include implementing automated calibration, expanding the angular scanning range, and integrating polarization control. For more complex or stochastic surfaces, scattering models such as Harvey and Shack or other statistical approaches could be introduced to derive roughness parameters more quantitatively. Additionally, combining angular scattering measurements with machine learning or high-throughput imaging techniques may enhance the system's capability for rapid surface classification and defect detection.

In summary, this work has shown that angle resolved scattering offers a powerful and accessible way to characterize microscale surface textures. It provides a direct link between optical response and morphological structure, and it opens possibilities for non-destructive and cost-effective surface evaluation in both research and applied contexts.

REFERENCES

[1] C. Bohren and D. R. Huffman, *Absorption and Scattering of Light by Small Particles*. Wiley Science Paperback Series, 1998.

[2] L. Reynolds, P. Borowicz, J. Caton, M. Crouse, C. Dahlen, and A. Ward, "Developmental Programming of Fetal Growth and Development," *Veterinary Clinics of North America - Food Animal Practice*, vol. 35, pp. 229–247, 2019, doi: 10.1016/j.cvfa.2019.02.006.

[3] J. van Dam, S. Abrahami, A. Yilmaz, Y. Gonzalez-Garcia, H. Terryn, and J. M. C. Mol, "Effect of surface roughness and chemistry on the adhesion and durability of a steel-epoxy adhesive interface," *Int J Adhes Adhes*, vol. 96, p. 102450, 2019, doi: 10.1016/j.ijadhadh.2019.102450.

[4] I. Bayneva, M. Garina, and Y. Potyagova, "MATERIALS FOR OPTICAL SYSTEMS LIGHTING DEVICES," *Spravochnik. Inzhenernyi zhurnal*, pp. 14–20, 2024, doi: 10.14489/hb.2024.03.pp.014-020.

[5] N. B. Zhong, X. Zhu, Q. Liao, Y. Wang, R. Chen, and Y. Sun, "Effects of surface roughness on optical properties and sensitivity of fiber-optic evanescent wave sensors," *Appl Opt*, vol. 52, pp. 3937–3945, 2013, doi: 10.1364/AO.52.003937.

[6] M. Florescu *et al.*, "Improving solar cell efficiency using photonic band-gap materials," *Solar Energy Materials and Solar Cells*, vol. 91, pp. 1599–1610, 2007, doi: 10.1016/j.solmat.2007.05.001.

[7] H. Atwater and A. Polman, "Plasmonics for Improved Photovoltaic Devices," *Nat Mater*, vol. 9, p. 865, 2010, doi: 10.1038/nmat2866.

[8] S. G. Johnson, A. Mekis, S. Fan, and J. D. Joannopoulos, "Molding the flow of light," *Comput Sci Eng*, vol. 3, pp. 38–47, 2001, doi: 10.1109/5992.963426.

[9] H. Horvath, “Gustav Mie and the scattering and absorption of light by particles: Historic developments and basics,” *J Quant Spectrosc Radiat Transf*, vol. 110, pp. 787–799, 2009, doi: 10.1016/j.jqsrt.2009.02.022.

[10] V. Šulc *et al.*, “Multi-Wavelength Angle-Resolved Scattering of Randomly Rough Surfaces Based on the Scalar Diffraction Theory,” *Coatings*, vol. 13, p. 1853, 2023, doi: 10.3390/coatings13111853.

[11] C. Pacholski *et al.*, “Antireflective subwavelength structures on microlens arrays—comparison of various manufacturing techniques,” *Appl Opt*, vol. 51, pp. 8–14, 2011, doi: 10.1364/AO.51.000008.

[12] L. Gong, Z.-S. Wu, M. Gao, and T. Qu, “Analysis of composite/difference field scattering properties between a slightly rough optical surface and multi-body defects,” *Appl Opt*, vol. 57, pp. 2165–2171, 2018, doi: 10.1364/AO.57.002165.

[13] A. Jilani, M. Abdel-wahab, and A. Hammad, “Advance Deposition Techniques for Thin Film and Coating,” 2017. doi: 10.5772/65702.

[14] V. Heiskanen and M. Hamblin, “Photobiomodulation: Lasers vs Light Emitting Diodes?,” *Photochemical & Photobiological Sciences*, vol. 17, 2018, doi: 10.1039/C8PP00176F.

[15] B. R. Dr C and B. Raj, “Study of engineering surfaces using laser-scattering techniques,” *Sadhana*, vol. 28, pp. 739–761, 2003, doi: 10.1007/BF02706457.

[16] S. Nayar, K. Ikeuchi, and T. Kanade, “Surface Reflection: Physical and Geometrical Perspectives,” *Pattern Analysis and Machine Intelligence, IEEE Transactions on*, vol. 13, pp. 611–634, 1991, doi: 10.1109/34.85654.

[17] W. Kapłonek and K. Nadolny, “Laser Methods based on an Analysis of Scattered Light for Automated, In-process Inspection of Machined Surfaces:

A review," *Optik - International Journal for Light and Electron Optics*, vol. 126, pp. 2764–2770, 2015, doi: 10.1016/j.ijleo.2015.07.009.

[18] S. Schröder, T. Herffurth, H. Blaschke, and A. Duparré, "Angle-resolved scattering: an effective method for characterizing thin-film coatings," 2010.

[19] M. Trost, S. Schröder, T. Feigl, A. Duparré, and A. Tünnermann, "Roughness characterization of large EUV mirror optics by laser light scattering," in *Optical Fabrication, Testing, and Metrology IV*, SPIE, Sep. 2011, p. 81690P. doi: 10.1117/12.896792.

[20] A. Aziz, H. Shaikh, A. Vighio, K. E. Taqvi, and B. Javed, "Microscopic Techniques for Nanomaterials Characterization: A Concise Review," *Microsc Res Tech*, vol. 88, 2025, doi: 10.1002/jemt.24799.

[21] J. C. Stover, *Optical Scattering: Measurement and Analysis*, 3rd ed. Bellingham, WA: SPIE Press, 2012.

[22] Š. Šustek *et al.*, "Characterization of randomly rough surfaces using angle-resolved scattering of light and atomic force microscopy," *Journal of Optics*, vol. 23, May 2021, doi: 10.1088/2040-8986/ac1f35.

[23] Y. Zhao, I. Wu, C.-F. Cheng, U. Block, G.-C. Wang, and T.-M. Lu, "Characterization of random rough surfaces by in-plane light scattering," *J Appl Phys*, vol. 84, pp. 2571–2582, May 1998, doi: 10.1063/1.368419.

[24] J. A. Jr and A. Lakhtakia, "Surface electromagnetic waves: A review," *Laser Photon Rev*, vol. 5, pp. 234–246, 2011, doi: 10.1002/lpor.200900050.

[25] C. Niu, T. Zhu, and Y. Lv, "Influence of Surface Morphology on Absorptivity of Light-Absorbing Materials," *International Journal of Photoenergy*, vol. 2019, pp. 1–9, 2019, doi: 10.1155/2019/1476217.

[26] I. Lindell and A. Sihvola, “Electromagnetic Wave Reflection from Surface with General Boundary Conditions,” 2017, doi: 10.48550/arXiv.1702.04986.

[27] A. Nzao, “Study of the Influence of Electromagnetic Waves on the Atomic Structure in Engineering Environments with High Radioactive Activity,” 2025. doi: 10.5772/intechopen.1010125.

[28] yu chieh Cheng *et al.*, “Beam focusing in reflection from flat chirped mirrors,” *Phys Rev A (Coll Park)*, vol. 87, 2013, doi: 10.1103/PhysRevA.87.045802.

[29] W. Bacsa, R. Bacsa, and T. Myers, “Microscopic Origin of the Index of Refraction,” 2020, pp. 65–83. doi: 10.1007/978-3-030-58983-7_5.

[30] Eugene Hecht, *Optics*, 5th Edition. Pearson, 2017.

[31] B. McParland, “Photon Interactions with Matter,” 2010, doi: 10.1007/978-1-84882-126-2_6.

[32] J. Guo, M. Šindelka, and N. Moiseyev, “Oscillating direct electric current formed by a resonant tunneling diode inside a cavity with periodically oscillating mirrors,” *J Chem Phys*, vol. 161, 2024, doi: 10.1063/5.0205463.

[33] H.-J. Li, M. Qin, L. Wang, Z. Xiang, R. Ren, and J. Hu, “Total absorption of light in monolayer transition-metal dichalcogenides by critical coupling,” *Opt Express*, vol. 25, pp. 31612–31621, 2017, doi: 10.1364/OE.25.031612.

[34] P. Wangyang, Q. Wang, X. Wan, K. Hu, and K. Huang, “Optical absorption enhancement in silicon square nanohole and hybrid square nanowire-hole arrays for photovoltaic application,” *Opt Commun*, vol. 294, pp. 377–383, 2013, doi: 10.1016/j.optcom.2012.12.040.

[35] S. Ponce-Alcántara, A. Arangú, and G. Sanchez, “The importance of optical characterization of PV backsheets in improving solar module power,” *Photovoltaics International*, 2014.

[36] E. Ivanova, W. Mueller, W. Rickert, and E. Vilchevskaya, “The Fresnel equations of classical and extended electrodynamics – a review,” *ZAMM - Journal of Applied Mathematics and Mechanics / Zeitschrift für Angewandte Mathematik und Mechanik*, vol. 105, 2025, doi: 10.1002/zamm.70016.

[37] F. Flory, L. Escoubas, and G. Berginc, “Optical properties of nanostructured materials: A review,” *J Nanophotonics*, vol. 5, p. 2502, 2011, doi: 10.1117/1.3609266.

[38] V. Gareyan and Z. Gevorkian, “Impact of surface roughness on light absorption,” *Phys Rev A (Coll Park)*, vol. 109, 2024, doi: 10.1103/PhysRevA.109.013515.

[39] S. Schröder, A. Duparré, L. Coriand, A. Tünnermann, D. Penalver, and J. Harvey, “Modeling of light scattering in different regimes of surface roughness,” *Opt Express*, vol. 19, pp. 9820–9835, 2011, doi: 10.1364/OE.19.009820.

[40] B. Stagg and T. Charalampopoulos, “Surface-roughness effects on the determination of optical properties of materials by the reflection method,” *Appl Opt*, vol. 30, pp. 4113–4118, 1991, doi: 10.1364/AO.30.004113.

[41] T. Vorburger, R. Silver, R. Brodmann, B. Brodmann, and J. Seewig, “Light Scattering Methods,” *Optical Measurements of Surface Topography*, pp. 287–311, 2011, doi: 10.1007/978-3-642-12012-1_12.

[42] G. S. He, H.-Y. Qin, and Q. Zheng, “Rayleigh, Mie, and Tyndall scatterings of polystyrene microspheres in water: Wavelength, size, and angle

dependences," *J Appl Phys*, vol. 105, pp. 023110–023110, 2009, doi: 10.1063/1.3068473.

[43] J. Shi, H. Wu, F. Yan, J. Yang, and X. He, "Experimental study on stimulated scattering of ZnO nanospheres dispersed in water," *Journal of Nanoparticle Research*, vol. 18, 2016, doi: 10.1007/s11051-016-3333-1.

[44] C. Balderas-Cabrera and R. Castillo, "Mie scattering theory applied to light scattering of large nonhomogeneous colloidal spheres," *J Chem Phys*, vol. 161, 2024, doi: 10.1063/5.0216489.

[45] K. Khan, K. Mnaymneh, H. Awad, I. Hasan, and T. Hall, "Optical wave propagation in photonic crystal metamaterials," *Applied Physics A*, vol. 117, pp. 629–634, 2014, doi: 10.1007/s00339-014-8713-8.

[46] P. Harding, "Photonic crystals modified by optically resonant systems," *J Phys E*, 2008.

[47] I. Belogorokhov *et al.*, "Study of the transport properties of organic semiconductors...," *Semiconductors*, vol. 45, pp. 1457–1461, 2011, doi: 10.1134/S1063782611110054.

[48] W. Cui, "Modern Electromagnetic Field Theory and Its Application in Future Wireless Communication," *J Phys Conf Ser*, vol. 2386, p. 12044, 2022, doi: 10.1088/1742-6596/2386/1/012044.

[49] Z. Jacob, L. Alekseyev, and E. Narimanov, "Optical Hyperlens: Far-field imaging beyond the diffraction limit," *Opt Express*, vol. 14, pp. 8247–8256, 2006, doi: 10.1364/OE.14.008247.

[50] M. Hudlička, "Propagation of electromagnetic waves in periodic structures," Charles University in Prague, Faculty of Mathematics and Physics, 2007. [Online]. Available:

https://www.researchgate.net/publication/200733231_Propagation_of_electromagnetic_waves_in_periodic_structures

[51] C. Y. Ho, B.-C. Chen, and Y.-H. Tsai, “Scattering signals of monochromatic light incident on a rectangular microchannel,” *Computers & Mathematics with Applications*, vol. 64, pp. 1514–1521, 2012, doi: 10.1016/j.camwa.2012.03.106.

[52] A. Serebryannikov, A. Cakmak, and E. Ozbay, “Multichannel optical diode with unidirectional diffraction relevant total transmission,” *Opt Express*, vol. 20, pp. 14980–14990, 2012, doi: 10.1364/OE.20.014980.

[53] A. Voronov *et al.*, “Development of an ultra-high resolution diffraction grating for soft x-rays,” *Proceedings of SPIE - The International Society for Optical Engineering*, vol. 6705, 2007, doi: 10.1117/12.732658.

[54] T. Hayashi, M. Michihata, and Y. Takaya, “Total Angle-Resolved Scattering: Characterization of Microlens Mold Surface,” *Procedia Eng*, vol. 19, pp. 132–137, 2011, doi: 10.1016/j.proeng.2011.11.091.

[55] P. Krüger, F. Da Pieve, and J. Osterwalder, “Real-space multiple scattering method for angle-resolved photoemission and valence-band photoelectron diffraction and its application to Cu (111),” *Phys Rev B Condens Matter*, vol. 20, 2011, doi: 10.1103/PhysRevB.83.115437.

[56] V. A. Sterligov *et al.*, “Elastic laser light scattering by GaAs surfaces,” 1999.

[57] A. Goodarzi *et al.*, “Laser Induced Periodic Surface Structured c-Si Solar Cell with more than 16% efficiency.,” in *2021 Conference on Lasers and Electro-Optics Europe and European Quantum Electronics Conference*, Optica Publishing Group, 2021, p. cm_p_16. [Online]. Available: https://opg.optica.org/abstract.cfm?URI=CLEO_Europe-2021-cm_p_16

[58] Z. T. Özkarslıgil, “Laser Induced Periodic Surface Structuring for Surface Enhanced Raman Spectroscopy,” Middle East Technical University, Ankara, Turkey, 2020.

[59] A. Akbiyik, “FABRICATION AND CHARACTERIZATION OF SERS SUBSTRATES VIA LASER INDUCED PHOTOCHEMICAL SURFACE ROUGHENING OF SILICON A THESIS SUBMITTED TO THE GRADUATE SCHOOL OF NATURAL AND APPLIED SCIENCES OF MIDDLE EAST TECHNICAL UNIVERSITY,” 2022.

[60] A. Akbıyık, N. Avishan, Ö. Demirtaş, A. K. Demir, E. Yüce, and A. Bek, “Laser Photochemical Nanostructuring of Silicon for Surface Enhanced Raman Spectroscopy,” *Adv Opt Mater*, vol. 10, no. 14, Jul. 2022, doi: 10.1002/adom.202200114.

[61] R. W. Schafer, “What is a savitzky-golay filter?,” *IEEE Signal Process Mag*, vol. 28, no. 4, pp. 111–117, 2011, doi: 10.1109/MSP.2011.941097.